

See discussions, stats, and author profiles for this publication at: <https://www.researchgate.net/publication/283236840>

Mechanisms and Performances of Na_{1.5}Fe_{0.5}Ti_{1.5}(PO₄)₃/C Composite as Electrode Material for Na-Ion Batteries

ARTICLE *in* THE JOURNAL OF PHYSICAL CHEMISTRY C · OCTOBER 2015

Impact Factor: 4.77 · DOI: 10.1021/acs.jpcc.5b07931

READS

106

6 AUTHORS, INCLUDING:



Ismael Saadoune

Cadi Ayyad University

92 PUBLICATIONS 2,056 CITATIONS

[SEE PROFILE](#)



Moulay Tahar Sougrati

French National Centre for Scientific Research

94 PUBLICATIONS 1,293 CITATIONS

[SEE PROFILE](#)



Rachid Hakkou

Cadi Ayyad University

48 PUBLICATIONS 234 CITATIONS

[SEE PROFILE](#)



K. Edström

Uppsala University

215 PUBLICATIONS 4,350 CITATIONS

[SEE PROFILE](#)

Mechanisms and Performances of NaFeTi(PO)/C Composite as Electrode Material for Na-Ion Batteries

Siham Difi, Ismael Saadoune, Moulay Tahar Sougrati, Rachid Hakkou, Kristina Edstrom, and Pierre-Emmanuel Lippens

J. Phys. Chem. C, Just Accepted Manuscript • DOI: 10.1021/acs.jpcc.5b07931 • Publication Date (Web): 15 Oct 2015

Downloaded from <http://pubs.acs.org> on October 29, 2015

Just Accepted

"Just Accepted" manuscripts have been peer-reviewed and accepted for publication. They are posted online prior to technical editing, formatting for publication and author proofing. The American Chemical Society provides "Just Accepted" as a free service to the research community to expedite the dissemination of scientific material as soon as possible after acceptance. "Just Accepted" manuscripts appear in full in PDF format accompanied by an HTML abstract. "Just Accepted" manuscripts have been fully peer reviewed, but should not be considered the official version of record. They are accessible to all readers and citable by the Digital Object Identifier (DOI®). "Just Accepted" is an optional service offered to authors. Therefore, the "Just Accepted" Web site may not include all articles that will be published in the journal. After a manuscript is technically edited and formatted, it will be removed from the "Just Accepted" Web site and published as an ASAP article. Note that technical editing may introduce minor changes to the manuscript text and/or graphics which could affect content, and all legal disclaimers and ethical guidelines that apply to the journal pertain. ACS cannot be held responsible for errors or consequences arising from the use of information contained in these "Just Accepted" manuscripts.



ACS Publications

The Journal of Physical Chemistry C is published by the American Chemical Society.

1155 Sixteenth Street N.W., Washington, DC 20036

Published by American Chemical Society. Copyright © American Chemical Society.

However, no copyright claim is made to original U.S. Government works, or works produced by employees of any Commonwealth realm Crown government in the course of their duties.

1
2
3
4
5 **Mechanisms and Performances of $\text{Na}_{1.5}\text{Fe}_{0.5}\text{Ti}_{1.5}(\text{PO}_4)_3/\text{C}$ Composite as**
6 **Electrode Material for Na-ion Batteries**

7
8
9
10
11
12
13 **Siham Difi^{1,2}, Ismael Saadoune², Moulay Tahar Sougrati^{1,3},**
14 **Rachid Hakkou², Kristina Edstrom⁴, Pierre-Emmanuel Lippens^{1,3,*}**

15
16
17
18 ¹ *Institut Charles Gerhardt, UMR 5253 CNRS, Université de Montpellier,
19 Place Eugène Bataillon, 34095 Montpellier cedex 5, France*

20
21
22
23
24 ² *Laboratoire de Chimie des Matériaux et de l'Environnement, Université Cadi Ayyad,
25 Avenue A. Khattabi, BP 549 Marrakech, Morocco*

26
27
28
29 ³ *Réseau sur le Stockage Electrochimique de l'Energie (RS2E), FR 3459 CNRS, France*

30
31
32
33 ⁴ *Department of Chemistry - Ångström laboratory, Uppsala University,
34 Box 538, SE 751 21, Uppsala, Sweden*

35
36
37 *Corresponding author: lippens@univ-montp2.fr

ABSTRACT

The properties, insertion mechanisms and electrochemical performances of $\text{Na}_{1.5}\text{Fe}_{0.5}\text{Ti}_{1.5}(\text{PO}_4)_3/\text{C}$ composite as electrode material for Na-ion batteries are reported. The composite was obtained by solid-state reaction and consists of porous secondary particles of submicron-sized particles coated by carbon. Detailed characterizations were performed by combining theoretical and experimental tools. This includes the determination of the crystal structure of $\text{Na}_{1.5}\text{Fe}_{0.5}\text{Ti}_{1.5}(\text{PO}_4)_3$ from both first-principles calculations and X-ray diffraction providing Na distribution over M1 and M2 interstitial sites, which is of importance for ionic conductivity. $\text{Na}_{1.5}\text{Fe}_{0.5}\text{Ti}_{1.5}(\text{PO}_4)_3/\text{C}$ was used as electrode material at 2.2 V *vs.* Na^+/Na^0 exhibiting good Na-storage ability with a specific capacity of 125 mAh g^{-1} , close to the theoretical value, for the first discharge at C/10, good capacity retention and coulombic efficiency of 95% and 99.5% at the 60th cycle, respectively, and high power rate with a decrease of the specific capacity of only 14% from C/10 to 2C. These good performances were related to the morphology of the composite and the substitution of Fe for Ti leading to an insertion mechanism that differs from that of $\text{NaTi}_2(\text{PO}_4)_3$. This mechanism was quantitatively analyzed from *operando* ^{57}Fe Mössbauer spectroscopy used for the first time in both galvanostatic and GITT modes.

Keywords: Electrode, Na-ion batteries, First-principles calculations, Mössbauer spectroscopy

1. Introduction

Electrochemical rechargeable batteries are considered as one of the leading technologies for electrical energy storage, especially for the development of sustainable and renewable energy sources, electric vehicles and portable electronic devices [1]. Li-ion batteries provide high energy density [2] but lithium resources are unevenly distributed worldwide and might not meet the increasing demand for energy [3]. In addition, cost and safety are major drawbacks, particularly for large-scale applications such as stationary energy storage systems [4]. In this light, rechargeable Na-ion batteries can be considered as a serious alternative because of the natural abundance and low cost of sodium, but also for the safety of the electrochemical systems that use, for example, aqueous electrolytes [5]. The main disadvantage of these batteries is the lower energy density compared to Li-ion batteries due to lower operation voltage and higher atomic mass of Na compared to Li. However, Na-ion batteries could be the best option for applications when cycle life and low cost are more essential factors than energy density.

Research on electrode materials has been mainly focused on Li-ion batteries and new cathode and anode materials with high specific capacity, low irreversible loss, high coulombic efficiency and long cycle life are needed for the development of Na-ion batteries [6-8]. Moreover, the electrode materials should be stable, abundant, inexpensive and environmentally benign. Even though, Na^+ ionic radius is larger than that of Li^+ , a lot of structures can accommodate Na^+ allowing fast diffusion at room temperature. As a result, Na-ion batteries can be competitive with Li-ion batteries in terms of charge-discharge rates. Positive electrodes, similar to those developed for Li-ion batteries, have been considered for a long time [9]. Layered oxides of the type Na_xMO_2 , where M represents one or more than one transition metals (M = V, Cr, Mn, Fe, Co, Ni) have been widely investigated since Na^+ can be easily intercalated between layers [10-11]. Transition metal oxides with open structures can also be used to reversibly insert Na, but polyanionic compounds form a particularly interesting family of positive electrode materials [12]. In this family, phosphate based

1
2
3 materials have attracted a considerable attention for several decades because of the diversity
4 of both their structures and properties including, for example, high ionic conductivity and the
5 possibility of tuning the operation voltage as a function of the type of transition metal.
6 NASICON (Na Super Ionic Conductors) type materials with the formula unit $A_xM_y(PO_4)_3$,
7 where A and M are alkali and metal atoms, respectively, can be described as three-
8 dimensional framework of corner sharing MO_6 octahedra and PO_4 tetrahedra with
9 interconnected channels for the diffusion of alkali ions. These materials exhibit high ionic
10 conductivity associated with low activation energy [13]. The NASICON phosphate structure
11 is often rhombohedral and can be viewed as a framework of corner sharing $M_2(PO_4)_3$ units
12 stacked parallel to the c hexagonal axis and connected to six other units with large interstitial
13 voids where the crystallographic sites M1 and M2 are located. There are one M1 and three
14 M2 sites per formula unit (f.u.) that can be occupied by Na. The initial occupation of these
15 sites in the pristine material determines the charge-discharge mechanism. The strongly
16 covalent PO_4 units that are responsible of inductive effects, the flexibility of the framework
17 formed by corner sharing octahedral and tetrahedral units as well as the large open channels,
18 provide structural stability and intrinsic safety even at high charge states [14].
19
20

21 Charge-discharge capabilities of the NASICON-type materials $NaTi_2(PO_4)_3$ were first
22 demonstrated by Delmas *et al* [15]. The reversible insertion mechanism is based on the two-
23 phase reaction $NaTi_2(PO_4)_3 \leftrightarrow Na_3Ti_2(PO_4)_3$. The potential curve is formed by a plateau at
24 about 2.1 V vs Na^+/Na^0 fixed by the redox potential of Ti^{4+}/Ti^{3+} and the theoretical specific
25 capacity is 132.8 mA h g⁻¹. $Na_3Ti_2(PO_4)_3$ has a monoclinic P-1 structure which is close to the
26 rhombohedral $R\bar{3}c$ structure of $NaTi_2(PO_4)_3$ making easier the two-phase reaction [15-17].
27 $NaTi_2(PO_4)_3$ is an interesting electrode material for Na-ion batteries. As an anode, the
28 potential of 2.1 V vs. Na^+/Na^0 is high enough to avoid the formation of a surface electrolyte
29 interphase (SEI) and as a cathode it can be used with a low potential anode. More
30 interestingly, the composition $Na_3Ti_2(PO_4)_3$ can be used in a symmetrical electrochemical cell
31 involving the reversible reactions $NaTi_2(PO_4)_3 \leftrightarrow Na_3Ti_2(PO_4)_3$ at the cathode and
32 $Na_3Ti_2(PO_4)_3 \leftrightarrow Na_4Ti_2(PO_4)_3$ at the anode since the latter transformation gives a potential
33 plateau at 0.6 V vs. Na^+/Na^0 due to the Ti^{3+}/Ti^{2+} redox couple [16]. As for most oxide
34
35
36
37
38
39
40
41
42
43
44
45
46
47
48
49
50
51
52
53
54
55
56
57
58
59
60

insertion materials, the electronic conductivity of $\text{NaTi}_2(\text{PO}_4)_3$ is too low for practical applications especially in terms of cycleability, power performances at high rates and polarization between charge and discharge potentials. Electronic percolation can be improved by conductive additives or by carbon coating of the particles that both enhance inter-particle conduction properties. In addition, decreasing the particle size or increasing porosity reduces the ionic and electronic pathways, which improves the electrochemical kinetics and increases the surface area in contact with electrolyte. Both carbon coating and nanostructuration can be made during synthesis with a carbon source in order to obtain a $\text{NaTi}_2(\text{PO}_4)_3/\text{C}$ composite. Different methods were previously proposed to obtain $\text{NaTi}_2(\text{PO}_4)_3$ or $\text{NaTi}_2(\text{PO}_4)_3/\text{C}$ with different morphologies and sizes: solid-state reaction [18] eventually followed by pyrolysis with a carbon source like glucose [19], high temperature reaction including citrate [20], solvothermal method combined with calcinations [21, 22], sol-gel method [23], hydrothermal technique [24] or microwave preparation [25].

The electrochemical properties of $\text{Na}_2\text{FeTi}(\text{PO}_4)_3$, obtained by solid state reaction were first reported by Tillement *et al* [26]. The potential curve of the first discharge obtained by these authors in galvanostatic mode at C/50 (1 Na/f.u. in 50 hours) shows a two-phase plateau at 2.3 V vs. Na^+/Na^0 until 0.5 inserted Na/f.u. followed by a continuous decrease until 1.5 V vs. Na^+/Na^0 for about 2 inserted Na/f.u. The incremental capacity curve shows peaks at 1 and 1.5 inserted Na/f.u. that were attributed to local orderings. A material with the same composition was also synthesized by solid state reaction, but with a somewhat different procedure, by Patoux *et al* [27]. The structure was accurately determined by neutron diffraction. The same rhombohedral space group ($R\bar{3}c$) as that of $\text{Na}_3\text{Ti}_2(\text{PO}_4)_3$ was obtained with slightly different lattice parameters. The potential curve obtained in galvanostatic regime at C/10 for the first cycle does not show neither a well-defined plateau as in the case of $\text{NaTi}_2(\text{PO}_4)_3$ nor a two-step mechanism as observed by Tillement *et al* [26] but a single-phase reaction. This result was also confirmed by potential intermittent titration technique (PITT) and by *in situ* X-ray diffraction (XRD). Recently, Aragon *et al* [28] used sol-gel method and citric acid as carbon source to obtain $\text{Na}_{1+x}\text{Fe}_x\text{Ti}_{2-x}(\text{PO}_4)_3/\text{C}$ composites with $x = 0, 0.2, 0.4$ and 0.6. For all the compositions, the structure is rhombohedral and the composites were

formed by aggregation of carbon-coated nanoparticles. The potential curves measured in galvanostatic mode at C/10 show a two-step reaction mechanism which differs from those described by Tillement *et al* [26] and by Patoux *et al* [27]. Along the discharge, there is a continuous decrease of the potential followed by a well-defined plateau at about 2.1 V *vs.* Na^+/Na^0 . The first domain is limited to about 0.1, 0.25 and 0.3 inserted Na/f.u. for $x = 0.2$, 0.4, 0.6, respectively, although the PITT curve for $x = 0.6$ shows a more extended domain until 0.6 inserted Na/f.u. In the latter case, the PITT curve exhibits a series of successive small plateaus characteristic of local Na orderings over the M2 interstitial sites. This first domain was attributed to change in Fe oxidation state from Fe^{3+} for the pristine material to Fe^{2+} based on *ex situ* ^{57}Fe Mössbauer experiments carried out for $x = 0.4$. For 1 inserted Na/f.u., the Fe^{2+} Mössbauer component represents only 80% of the total spectrum area, which indicates that although most of the Fe^{3+} were reduced in the first half of the discharge, there is no clear evidence that this change took place only in the first domain (< 0.4 inserted Na/f.u.). The authors pointed out that substitution of Fe for Ti improves electrochemical performances compared to $\text{Na}_3\text{Ti}_2(\text{PO}_4)_3$. The specific capacities of the first discharge were found to be 120, 130, 119 and 117 mAh g⁻¹ and the coulombic efficiency were 79%, 91%, 87% and 85% for $x = 0, 0.2, 0.4, 0.6$, respectively. The observed decrease of the capacity with increasing $x \geq 0.2$ was attributed to the increase of Na amount in the pristine material. Improved capacity retention and power rate were also observed with a Coulombic efficiency in the range 85-92 % and a decrease of the capacity lower than 10% from C/10 to C/2 that have been related to low internal impedance. Thus, the comparison of the results obtained by these authors suggests that different insertion mechanisms operate in Fe-Ti based NASICON electrode material for Na-ion batteries that do not only depend on the composition but also on other aspects of the pristine material like crystallinity, particle size, carbon coating, etc. This also depends on the experimental conditions used for electrochemical tests as observed, for example, from the differences between galvanostatic and PITT results that could be due to kinetic effects [28].

The present work concerns the electrochemical performances of $\text{Na}_{1.5}\text{Fe}_{0.5}\text{Ti}_{1.5}(\text{PO}_4)_3/\text{C}$ composite as electrode material for Na-ion batteries with operating

voltage of 2.2 V vs. Na^+/Na^0 . The composite was obtained by solid state reaction and sucrose pyrolysis and was characterized by different experimental and theoretical tools. First, the results of first-principles structural optimization of $\text{NaTi}_2(\text{PO}_4)_3$, considered as reference material, and $\text{Na}_{1.5}\text{Fe}_{0.5}\text{Ti}_{1.5}(\text{PO}_4)_3$ are presented. They give a validation of the experimental structure obtained by XRD and provide additional information to help the experimental characterization. Then, an atomic-scale experimental study of $\text{Na}_{1.5}\text{Fe}_{0.5}\text{Ti}_{1.5}(\text{PO}_4)_3$ and $\text{Na}_{1.5}\text{Fe}_{0.5}\text{Ti}_{1.5}(\text{PO}_4)_3/\text{C}$ based on ^{57}Fe Mössbauer spectroscopy, magnetic measurements and Raman spectroscopy is reported as well as the characterization of the material morphology from electron microscopy and surface area measurements. This highlights the effect of sucrose pyrolysis. It also seems important to propose an analysis of the effect of the Fe substitution for Ti on Na^+ insertion mechanism based on electrochemistry techniques and ^{57}Fe Mössbauer spectroscopy in *operando* mode which is a very efficient tool to follow such reaction mechanisms [29, 30]. Finally, the electrochemical performances of $\text{Na}_{1.5}\text{Fe}_{0.5}\text{Ti}_{1.5}(\text{PO}_4)_3/\text{C}$ are detailed and compared to previously published works on similar systems.

2. Experimental and theoretical methods

2.1 Synthesis

$\text{Na}_{1.5}\text{Fe}_{0.5}\text{Ti}_{1.5}(\text{PO}_4)_3$ was prepared by solid-state reaction. Stoichiometric amounts of Na_2CO_3 (99.5% Sigma-Aldrich), $(\text{NH}_4)_2\text{HPO}_4$ (99.9% Sigma-Aldrich), Fe_2O_3 (99.9% Sigma-Aldrich), and TiO_2 (99.5% Fischer) were ball-milled in order to obtain a finely ground and homogeneous mixed powder. Subsequently, the powder was heated at 400°C under air for 12 h in an open alumina crucible and cooled to room temperature. The product was then hand-ground and heated at 600°C for 12 h and, after cooling at room temperature, reground and calcined at 1000°C for 12 h to obtain pure powder of $\text{Na}_{1.5}\text{Fe}_{0.5}\text{Ti}_{1.5}(\text{PO}_4)_3$. For carbon coating, the $\text{Na}_{1.5}\text{Fe}_{0.5}\text{Ti}_{1.5}(\text{PO}_4)_3$ powder was mixed with 15 wt% of sucrose powder in acetone. The solution was then dried for the evaporation of acetone and heated at 500°C for 6 h in flowing argon. The final product was a black powder of $\text{Na}_{1.5}\text{Fe}_{0.5}\text{Ti}_{1.5}(\text{PO}_4)_3/\text{C}$.

1
2
3 composite. For comparison, iron free NaTi₂(PO₄)₃/C was prepared with the same method
4 except that Fe₂O₃ was not used in the process.
5
6
7
8
9

10 **2.2 X-ray diffraction**

11 The X-ray diffraction (XRD) patterns were collected under Bragg-Brentano geometry
12 at 20 in the range 12-120° with a step of 0.02° and 30 s for each step. The XRD experiments
13 were performed at room temperature with PHILIPS X’Pert MPD equipped with the
14 X’celerator detector using Ni filter and Cu-K α radiation ($\lambda = 1.5418 \text{ \AA}$). The structural
15 parameters were obtained from the diffraction patterns with the Rietveld method [31] using
16 the FULLPROF program [32]. The refinement of the structure was performed using a pseudo-
17 Voigt profile function to describe the shape of the diffraction lines. The microstructure was
18 analyzed with a scanning electron microscope (SEM) and a transmission electron microscope
19 (TEM) for high resolution images. The specific surface areas of the powdered samples were
20 evaluated with the Brunauer Emmett Teller (BET) method from nitrogen physisorption
21 measurements at 77 K with a Micrometric ASAP 2020. The residual carbon content was
22 determined from thermogravimetric analysis (TGA) with a heating rate of 10°C min⁻¹ using a
23 thermal analyzer Labsys.
24
25

26 **2.3 Raman spectroscopy**

27 The Raman scattering spectra were recorded in the 100–2000 cm⁻¹ range, at room
28 temperature using a LabRAM ARAMIS IR² spectrometer equipped with a 632 nm laser
29 diode, a 1200 gr mm⁻¹ grating with X50 long work distance objective. Each spectrum was
30 recorded with an acquisition time of 30 min.
31
32

33 **2.4 Magnetic measurements**

34 The magnetic susceptibility was measured with a Superconducting Quantum
35 Interference Design (SQUID) magnetometer MPMS XL7. The samples were first cooled to 2
36 K under zero magnetic field (ZFC). Then, a magnetic field of 100 mT was applied and the
37 susceptibility was recorded from 2 to 300 K. Finally, the susceptibility was also measured by
38 cooling the samples to 2 K with the same field (FC).
39
40

41 **2.5 Mössbauer spectroscopy**

The ^{57}Fe Mössbauer spectra were recorded in transmission geometry and a constant acceleration mode at room temperature with ^{57}Co (Rh) as γ source. The velocity scale was calibrated using the magnetic six-line spectrum of a high-purity iron foil absorber as a standard. The values of isomer shift (δ), quadrupole splitting (Δ), full linewidth at half maximum (Γ) and relative area (RA) were determined by fitting Lorentzian lines to experimental data with a non-linear least square method. The values of the isomer shift (δ) are given with respect to $\alpha\text{-Fe}$ and the goodness of the fits was controlled by a classical χ^2 test.

2.6 Electrochemical measurements

The electrochemical tests were performed in coin cells. The working electrodes were prepared by mixing 75 wt% active material, 15 wt% Super P carbon powder and 10 wt% PVDF (polyvinylidene fluoride) binder in NMP (1-methyl-2-pyrrolidinone). The mixture was spread on Al foil substrate and dried at 120°C for 12 h under vacuum to remove solvent and water. Coin cells were assembled inside filled dry box under controlled argon atmosphere by using a sodium foil as counter electrode, a borosilicate glass microfiber sheet (Whatman) as separator and an organic electrolyte with 1M NaClO_4 dissolved in a solution of propylene carbonate (PC) and 5 vol% of fluoroethylene carbonate (FEC) as additive. The cells were cycled in a voltage range between 1.6 and 3.0 V, under galvanostatic conditions with C/n current rate (1 Na/f.u. in n hours), where n=10, 5, 2, 1, 0.2.

A specific electrochemical cell was used for *in situ* ^{57}Fe Mössbauer spectroscopy in transmission mode [33]. Two methods were considered to study changes in Fe oxidation state during charge-discharge cycles. In the first one, the *operando* Mössbauer data were collected along the first cycle performed in galvanostatic mode at C/25 during time steps of 5 h. Thus, each spectrum corresponded to the insertion (discharge) or extraction (charge) of 0.2 Na/f.u. However, the evaluation of the hyperfine parameters was made difficult by the rather poor signal-to-noise ratio due to the small amount of ^{57}Fe (natural abundance: 2.12 %) in the electrode material and only the relative contributions of the two oxidation states to the whole spectra were evaluated. The other method was based on GITT mode in order to record *in situ* Mössbauer spectra at equilibrium potentials. This allowed to reduce the influence of the kinetic effects and increase the recording time without increasing the number of inserted Na

as in galvanostatic mode. In that case, one full discharge-charge cycle and the second discharge were conducted at C/10, interrupted every 4 h for the first cycle and every 1 h for the second discharge by relaxation periods of 12 hours to collect the *in situ* Mössbauer data.

2.7 Theoretical method

The theoretical structural optimizations of $\text{NaTi}_2(\text{PO}_4)_3$ and $\text{Na}_{1.5}\text{Fe}_{0.5}\text{Ti}_{1.5}(\text{PO}_4)_3$ were performed with the pseudopotential method as implemented in CASTEP code [34] based on the density functional theory (DFT) [35, 36] and the generalized-gradient approximation (GGA) using an exchange-correlation potential by Perdew, Burke, and Ernzerhof for solids (PBE SOL) [37]. Ultrasoft pseudopotentials [38] and the reciprocal space representation were used. For $\text{Na}_{1.5}\text{Fe}_{0.5}\text{Ti}_{1.5}(\text{PO}_4)_3$ a supercell of 37 atoms was used with $P1$ space group in order to fully relax all the atomic positions. All the different configurations of Na atoms within the interstitial sites M1 and M2 were considered. The plane-wave kinetic-energy cutoff was set to 400 eV and the k-space sampling was performed on a Monkhorst-Pack grid with 14 k points in the irreducible wedge of the Brillouin zone. Both the lattice parameters and the atom positions were relaxed until the mechanical equilibrium was achieved through conjugate-gradient minimization of the total energy to a tolerance of 10^{-5} eV/atom, the forces to a tolerance of 0.03 eV \AA^{-1} , the stress to a tolerance of $5 \cdot 10^{-2}$ GPa and the atomic positions to a tolerance of 10^{-3} \AA . For the two most stable configurations of Na atoms, the convergence of the structural parameters was checked by increasing the energy cutoff (800 eV) and the number of k points (32 k) while the convergence parameters were changed to 10^{-6} eV/atom, $5 \cdot 10^{-3}$ eV \AA^{-1} , 10^{-2} GPa and $2 \cdot 10^{-4}$ \AA . A density-mixing scheme with a conjugate-gradient Pulay solver was used for the energy minimization and a BFGS algorithm for the internal-coordinate optimization. The ^{57}Fe Mössbauer parameters of $\text{Na}_{1.5}\text{Fe}_{0.5}\text{Ti}_{1.5}(\text{PO}_4)_3$ were evaluated with the linearized augmented plane-wave method (LAPW) as implemented in the WIEN2k code [39] by considering the structural parameters of the most stable phase obtained from pseudopotential calculations. With this method, the unit cell is partitioned into atomic spheres centered at the atomic positions and an interstitial region. The muffin-tin radii of the atomic spheres were $R_{\text{mt}}(\text{Na}) = 2.2$ a.u., $R_{\text{mt}}(\text{Fe}) = 2.0$ a.u., $R_{\text{mt}}(\text{Ti}) = 2.0$ a.u., $R_{\text{mt}}(\text{P}) = 1.4$ a.u. and $R_{\text{mt}}(\text{O}) = 1.4$ a.u. To improve the energy linearization, the basis set was extended with local

1
2
3 orbitals. In the interstitial region, the wave functions were expanded in plane waves with
4 wavenumbers k such as $\text{min}(\text{Rmt}).\text{max}(k) = 8$ and the charge density was expanded in a
5 Fourier series with $G_{\text{max}} = 16 \text{ Ry}^{1/2}$.
6
7
8
9
10

11 **3. Results and discussion** 12

13 **3.1 Theoretical structure of the pristine material** 14

15 It has been reported previously that $\text{Na}_{1+x}\text{Fe}_x\text{Ti}_{2-x}(\text{PO}_4)_3$ compounds with $0 \leq x \leq 1$ are
16 isostructural to $\text{NaTi}_2(\text{PO}_4)_3$ [26-28]. The structure of $\text{NaTi}_2(\text{PO}_4)_3$ can be described in the
17 rhombohedral system (space group $R\bar{3}c$, n°167). The rhombohedral primitive cell contains 36
18 atoms ($Z=2$). In the most commonly used hexagonal description, Ti and P are in 12c and 18e
19 Wickoff positions, respectively, and there are two different crystallographic sites for the
20 oxygen atoms, O(1) and O(2), both in 36f Wyckoff positions. The structure consists of a
21 three-dimensional framework of corner sharing PO_4 tetrahedra and TiO_6 octahedra which are
22 both slightly distorted. There are two possible types of interstitial sites that can be occupied
23 by Na: M1 in 6b and M2 in 18e Wickoff positions, respectively. The M1 site is surrounded by
24 6 O first-nearest neighbors forming a distorted octahedron. These O atoms belong to the
25 triangular faces of two adjacent TiO_6 octahedra along the hexagonal c axis. The M2 sites are
26 located between the PO_4 tetrahedra and have 8 O first-nearest neighbors that form a strongly
27 distorted polyhedron. The published experimental lattice parameters are found in the ranges
28 $a_{\text{hex}} = 8.48 \pm 0.01 \text{ \AA}$ and $c_{\text{hex}} = 21.80 \pm 0.02 \text{ \AA}$ depending on the synthesis method and the
29 experimental conditions of measurements [16, 40, 41]. This gives a rhombohedral unit cell
30 volume $V_{\text{rho}} = 452.5 \pm 1.5 \text{ \AA}^3$. The Rietveld refinement of the XRD pattern of $\text{NaTi}_2(\text{PO}_4)_3$
31 synthesized in this work with the same method as $\text{Na}_{1.5}\text{Fe}_{0.5}\text{Ti}_{1.5}(\text{PO}_4)_3$ has provided similar
32 values of the lattice parameters and a cell volume of 452.5 \AA^3 in agreement with published
33 results (Table 1).
34

35 DFT calculations were first performed for $\text{NaTi}_2(\text{PO}_4)_3$ in order to test the accuracy of
36 the theoretical method to determine the most stable configuration of the Na atoms in the M1
37 and M2 interstitial sites and to evaluate the structural parameters. There are 28 possibilities to
38

place the 2 Na atoms over the 8 interstitial sites of the rhombohedral cell of $\text{NaTi}_2(\text{PO}_4)_3$. However, only several starting configurations have been considered because of the symmetries of the initial rhombohedral primitive cell. Previously published experimental lattice parameters and atomic positions obtained for $\text{NaTi}_2(\text{PO}_4)_3$ [41] were used as starting values of the structural optimizations except for Na in M2 where the coordinates (0.65, 0, 0.25) close to those obtained for $\text{Na}_2\text{FeTi}(\text{PO}_4)_3$ [27] were considered. Based on the total energy values obtained for the optimized structures, three types of Na configurations were distinguished: 2 Na in M1, 1 Na in M1 and 1 Na in M2, 2 Na in M2. The total energy obtained for Na in M1 was about 0.3 eV/f.u. lower than that obtained for Na in both M1 and M2 and about 0.5 eV/f.u. lower than that obtained for Na in only M2. This clearly indicates that the most stable $\text{NaTi}_2(\text{PO}_4)_3$ phase predicted by DFT is obtained with the full occupation of the M1 sites by Na in agreement with previously published experimental data. In addition, the theoretical volumes of the rhombohedral primitive cells are 456.2, 461.7 and 466.7 Å³ for M1, M1+M2 and M2 occupations, respectively. The comparison with the averaged experimental value (452.5 Å³) indicates that the best agreement is also obtained for Na in M1. This agreement is slightly better by considering improved computational parameters (see Section 2) since, in this case, the rhombohedral cell volume is: $V_{\text{rho}} = 455.9 \text{ \AA}^3$, which overestimates the experimental volume by less than 1%. The theoretical atomic positions and the main interatomic distances of the most stable phase are similar to the experimental data obtained in this work (Table 1). It is worth noting that such an excellent agreement was obtained with the PBESOL functional. Moreover, GGA and LDA calculations were also performed with the functionals of Perdew, Burke and Ernzerhof (PBE) [42] and Perdew and Zunger (PZ) [43], respectively. In the two cases, the most stable Na configuration is the same as that obtained with the PBESOL functional. However, the rhombohedral cell volumes were found to be 465.6 Å³ (PBE) and 438.8 Å³ (PZ), which overestimates and underestimates the experimental volume by about 3%, respectively. Finally, the effect of Ti 3d electron correlation was checked by a GGA (PBESOL) + U spin polarized calculation, with U = 4 eV. The calculated rhombohedral cell volume (459.1 Å³) is slightly higher than that obtained with U = 0 eV, which does not improve the agreement with the experimental value. These results

show the high accuracy of the DFT-PBESOL method for the geometry optimization of $\text{NaTi}_2(\text{PO}_4)_3$, which justifies its use for the structural analysis of the substitution of Fe for Ti in this compound.

A supercell of 37 atoms with the composition $\text{Na}_3\text{FeTi}_3(\text{PO}_4)_6$ was considered for the structural optimization of $\text{Na}_{1.5}\text{Fe}_{0.5}\text{Ti}_{1.5}(\text{PO}_4)_3$. The lattice parameters and the atomic positions of the rhombohedral cell of $\text{NaTi}_2(\text{PO}_4)_3$ were used to initialize the calculations but one Ti atom was replaced by Fe in the supercell and relaxation of all the atoms was allowed by considering the *P*1 space group. There are 56 possible distributions of the 3 Na atoms over the 2 M1 and 6 M2 sites (3 sites close to Fe: M2/Fe and 3 sites close to Ti: M2/Ti) among them some are equivalent due to the symmetry of the starting supercells. All the calculations provided high spin Fe^{3+} whatever the Na distribution. The most stable configuration was obtained with 3 Na atoms in the 2 M1 sites and in 1 M2 site close to Fe (M2/Fe). However, the total energy is only 0.065 eV/f.u. lower than that obtained with Na in the 2 M1 sites and in 1 M2/Ti site. The values of the total energy for the different configurations of Na in M1 + 2 M2 sites are about 0.2-0.4 eV/f.u. higher than those with Na in 2 M1+M2/Fe while the values for the configurations of Na in 3 M2 sites are about 0.3-0.6 eV/f.u. higher than those with Na in 2 M1+M2/Fe. The supercell volumes are about 462 \AA^3 (461 \AA^3 with improved computational parameters) for Na in 2 M1+M2, $466\text{-}470 \text{ \AA}^3$ for Na in M1+2 M2 and $473\text{-}480 \text{ \AA}^3$ for Na in 3 M2. Thus, the most stable Na configuration was obtained with fully occupied M1 sites and Na in a M2 site close to the FeO_6 octahedra. For a comparison with $\text{NaTi}_2(\text{PO}_4)_3$ and the experimental data, the theoretical structural parameters of an equivalent $R\bar{3}c$ crystal were evaluated from the *P*1 optimized supercell with improved computational parameters by averaging the lattice parameters and atomic coordinates (Table 2).

The theoretical rhombohedral cell volume of the most stable configuration obtained for $\text{Na}_{1.5}\text{Fe}_{0.5}\text{Ti}_{1.5}(\text{PO}_4)_3$ is 5 \AA^3 higher than the theoretical volume of $\text{NaTi}_2(\text{PO}_4)_3$. This increase of 1 % is due to the increase of a_{hex} (and b_{hex}) from 8.521 \AA for $\text{NaTi}_2(\text{PO}_4)_3$ to 8.582 \AA since c_{hex} decreases from 21.748 \AA for $\text{NaTi}_2(\text{PO}_4)_3$ to 21.685 \AA . These changes are rather small but reflect a significant trend in the lattice parameters that was experimentally observed for other Fe contents [27, 28]. The decrease of c_{hex} is mainly due to the decrease of the ionic

charge from Ti^{4+} to Fe^{3+} , which lowers the repulsive interactions between the transition metal cations that are located along the c_{hex} axis. As a result, the Fe-Ti and Fe-Na(M1) interatomic distances along c_{hex} in $\text{Na}_{1.5}\text{Fe}_{0.5}\text{Ti}_{1.5}(\text{PO}_4)_3$ are smaller than those of Ti-Ti and Ti-Na(M1) in $\text{NaTi}_2(\text{PO}_4)_3$, respectively (Fig. 1a). Due to local relaxations, all the bond lengths and bond angles in $\text{Na}_{1.5}\text{Fe}_{0.5}\text{Ti}_{1.5}(\text{PO}_4)_3$ are distributed leading to local distortions (Table 3). As an illustrative example, the FeO_6 local environment shows significant variations from perfect octahedron (Fig. 1b). The average values of Ti-O and Fe-O interatomic distances in TiO_6 and FeO_6 octahedra are 1.94 Å and 2.00 Å, respectively. This increase is in line with that of the ionic radius from 0.605 Å for Ti^{4+} to 0.645 Å for Fe^{3+} . The average P-O and Na(M1)-O interatomic distances are close to those in $\text{NaTi}_2(\text{PO}_4)_3$ but there are local distortions around Na(M1) and Na(M2) (Table 3). These local changes induced by the substitution of Fe for Ti and the occupation of M2 by Na increase the interatomic distances between the O atoms with close c_{hex} coordinates. This explains the increase of the lattice parameters a_{hex} and b_{hex} .

3.2 Experimental characterization of the pristine material

The X-ray diffraction pattern of $\text{Na}_{1.5}\text{Fe}_{0.5}\text{Ti}_{1.5}(\text{PO}_4)_3$ was indexed in the rhombohedral system with the space group $R\bar{3}c$ (Fig. 2a). There are no additional peaks that could be assigned to impurities or to long-range ordering involving Ti and Fe. The Rietveld refinement of the structure was initialized with the experimental lattice parameters and the atomic positions obtained in this work for $\text{NaTi}_2(\text{PO}_4)_3$ and the same M2 coordinates (0.65, 0, 0.25) used for DFT calculations. In addition, the relative occupations of the 12c sites with 25 at% Fe and 75 at% Ti, the M1 sites with 100 at% Na and the M2 sites with 17 at% Na were considered for the initialization. An overall correct agreement is obtained between the experimental (Table 4) and theoretical (Table 2) values of the lattice constants and atomic coordinates. For example, the experimental volume of the rhombohedral cell (456.8 \AA^3) is only 1 % lower than the theoretical one (461.0 \AA^3). In addition, the theoretical increase of 1.05 % of the unit cell volume from $\text{NaTi}_2(\text{PO}_4)_3$ to $\text{Na}_{1.5}\text{Fe}_{0.5}\text{Ti}_{1.5}(\text{PO}_4)_3$ matches the present experimental value of 0.95 %. Finally, the experimental occupation rates of Ti, Fe and Na are close to the predicted values. This is a clear indication of the accuracy of the theoretical model and confirms the validity of our structural analysis given above, including the random

1
2
3 substitution of Fe for Ti and the Na occupation of the M1 and M2 sites. The XRD pattern of
4 the composite $\text{Na}_{1.5}\text{Fe}_{0.5}\text{Ti}_{1.5}(\text{PO}_4)_3/\text{C}$ is similar to that of the crystalline phase
5 $\text{Na}_{1.5}\text{Fe}_{0.5}\text{Ti}_{1.5}(\text{PO}_4)_3$ (Fig. 2b). There are no additional peaks due to the sucrose pyrolysis that
6 could be assigned to crystalline impurities. The structural parameters obtained from Rietveld
7 refinement are close to those of the pure crystalline phase and are not reported here.
8
9

10
11
12
13 The ^{57}Fe Mössbauer spectrum of $\text{Na}_{1.5}\text{Fe}_{0.5}\text{Ti}_{1.5}(\text{PO}_4)_3$ measured at room temperature
14 was fitted with a symmetrical doublet (Fig. 3a). The small linewidth indicates that Fe local
15 environments are similar within the overall crystalline phase (Table 5). The values of the
16 isomer shift: $0.437(1) \text{ mm s}^{-1}$ and the quadrupole splitting: $0.326(2) \text{ mm s}^{-1}$ are close to
17 previously published values for iron based NASICON compounds and can be assigned to high
18 spin Fe^{3+} ions in slightly distorted FeO_6 octahedra [44-46]. Higher values of the quadrupole
19 splitting ($\sim 0.8 \text{ mm s}^{-1}$) were recently reported for $\text{Na}_{1+x}\text{Fe}_x\text{Ti}_{2-x}(\text{PO}_4)_3$ with $x \leq 0.6$ [28]. To
20 confirm the present value, LAPW calculations of the electric field gradients at the Fe Nucleus
21 were performed for the theoretically optimized $P1$ supercell obtained for the most stable Na
22 configuration with the pseudopotential method. The theoretical approach is described in
23 section 2 and was previously used for different Mössbauer isotopes [47-51]. The quadrupole
24 splitting is given by
25
26

$$\Delta = \frac{1}{2} e Q V_{zz} \left(1 + \frac{\eta^2}{3} \right)^{1/2} \quad (1)$$

27
28
29 where e is the electron charge, Q is the ^{57}Fe nuclear quadrupole moment of the first excited
30 state ($I = 3/2$), V_{zz} is the main component of the diagonalized EFG tensor, and η is the
31 asymmetry parameter defined by
32
33

$$\eta = \frac{V_{xx} - V_{yy}}{V_{zz}} \quad (2)$$

34
35 where V_{xx} and V_{yy} are the other two components of the diagonalized EFG tensor with $V_{xx} <$
36 $V_{yy} < V_{zz}$. We obtained $V_{zz} = 0.9 \text{ V m}^{-2}$ and $\eta = 0.63$, which gives $\Delta = 0.16 \text{ mm s}^{-1}$ by
37 considering $Q = 0.16 \text{ b}$ [52]. To take into account the Fe 3d electron correlation, we also
38 performed a GGA+U calculation which gave $V_{zz} = 1.9 \text{ V m}^{-2}$ and $\eta = 0.62$, leading to $\Delta =$
39 0.32 mm s^{-1} in better agreement with the present experimental value. In the two cases, the
40
41
42
43
44
45
46
47
48
49
50
51
52
53
54
55
56
57
58
59
60

rather small value of Δ originates from the weak asymmetry of the electronic density around Fe. This is due to the weak distortion of the FeO_6 octahedral environment (Fig. 1b) and to the high spin Fe^{3+} electronic configuration. This result confirms the present interpretation of the Mössbauer spectrum. The recently published higher values of Δ could be due to the small size of the particles obtained by sol-gel method, which provides higher surface-to-bulk ratio and more asymmetrical Fe local environments, or to structural disorder [46]. The ^{57}Fe Mössbauer spectrum of the composite $\text{Na}_{1.5}\text{Fe}_{0.5}\text{Ti}_{1.5}(\text{PO}_4)_3/\text{C}$ shows an additional small peak at about 2.37 mm s^{-1} and was fitted with two doublets (Fig. 3b). The Mössbauer parameters of the main doublet (91% relative area): $\delta = 0.420(7) \text{ mm s}^{-1}$ and $\Delta = 0.275(5) \text{ mm s}^{-1}$ are close to those of $\text{Na}_{1.5}\text{Fe}_{0.5}\text{Ti}_{1.5}(\text{PO}_4)_3$ while the isomer shift of the small doublet (9% relative area): $\delta = 1.178(7) \text{ mm s}^{-1}$ is typical of high spin Fe^{2+} (Table 5). The high value of the quadrupole splitting obtained for the latter doublet: $\Delta = 2.368(2) \text{ mm s}^{-1}$ indicates a strong anisotropy of the electron density around Fe. This is mainly due to the partial occupation of the Fe 3d spin down states but could also be related to more distorted Fe local environment. This additional component arose from sucrose pyrolysis and could be related to intrinsic defects or external impurities such as olivine Na_xFePO_4 , the Mössbauer parameters of which being close to the present values for Fe^{2+} [53]. The absence of additional XRD peaks is in favor of intrinsic defects or impurities with small size and/or amorphous. Whatever its exact nature, this defect will be called “ Fe^{2+} impurity” later in this paper and its influence upon the reaction mechanism and electrochemical performances will be analyzed in the section 4.

The inverse magnetic susceptibility of $\text{Na}_{1.5}\text{Fe}_{0.5}\text{Ti}_{1.5}(\text{PO}_4)_3$ progressively increases with temperature from the origin and follows a Curie-Weiss law above about 30 K (Fig. 4). This curve differs from that of $\text{Na}_3\text{Fe}_2(\text{PO}_4)_3$ which shows a typical antiferromagnetic order at low temperature below the Néel temperature of 47 K [46, 54]. The present Curie temperature: $\theta_{\text{NFTP}} = -8 \text{ K}$ is close to 0 K and strongly differs from that of $\text{Na}_3\text{Fe}_2(\text{PO}_4)_3$ at -85 K [46]. This clearly indicates that antiferromagnetic order is negligible in our samples and confirms that Fe atoms are randomly distributed over the 12c sites and do not form inhomogeneous regions of high Fe concentration. The value of the Curie constant, $C_{\text{NFTP}} = 3.67 \text{ emu K mol}^{-1}$, gives a magnetic moment $\mu_{\text{eff}} = 5.4 \mu_B$ per Fe atom, which is in the range of the published values

from 5.2 to 5.7 μ_B [46, 54]. This value is typical of high spin Fe^{3+} in octahedral FeO_6 environment and is lower than the spin-only value of Fe^{3+} free ion (5.9 μ_B). The variations of the inverse magnetic susceptibility of the $Na_{1.5}Fe_{0.5}Ti_{1.5}(PO_4)_3/C$ composite are similar to those of $Na_{1.5}Fe_{0.5}Ti_{1.5}(PO_4)_3$ except for a small decrease of the Curie constant: $C = 3.57 \text{ emu K mol}^{-1}$ leading to a magnetic moment $\mu_{\text{eff}} = 5.34 \mu_B$ per Fe atom. If we consider, for simplicity, that the magnetization of the composite originates only from those of $Na_{1.5}Fe_{0.5}Ti_{1.5}(PO_4)_3$ and Fe^{2+} impurity, the Curie-Weiss law in the paramagnetic regime can be written:

$$\chi = \frac{C}{T - \theta} = 0.91 \frac{C_{NFTP}}{T - \theta_{NFTP}} + 0.09 \frac{C_{Fe^{2+}}}{T - \theta_{Fe^{2+}}} \quad (3)$$

where $C_{Fe^{2+}}$ and $\theta_{Fe^{2+}}$ denote the Curie constant and the Curie temperature of the Fe^{2+} impurity, respectively. Since the Curie temperatures of $Na_{1.5}Fe_{0.5}Ti_{1.5}(PO_4)_3$ and $Na_{1.5}Fe_{0.5}Ti_{1.5}(PO_4)_3/C$ are very close, we have considered, for simplicity, that all the Curie temperatures are identical in Eq. 3 and obtained $C_{Fe^{2+}} = 2.56 \text{ emu K mol}^{-1}$. The resulting magnetic moment, $\mu_{\text{eff}} = 4.5 \mu_B$ per Fe atom, is lower than the spin-only magnetic moment of Fe^{2+} (4.9 μ_B). This result confirms the existence of high spin Fe^{2+} in the composite as observed from Mössbauer spectroscopy.

The SEM images show that $Na_{1.5}Fe_{0.5}Ti_{1.5}(PO_4)_3$ particles have an average size of several micrometers and rather smooth surfaces (Fig. 5a) while $Na_{1.5}Fe_{0.5}Ti_{1.5}(PO_4)_3/C$ is composed by micrometer sized secondary particles formed by the aggregation of smaller particles of several hundred nanometers (Fig. 5b). This indicates that sucrose pyrolysis produced porosity and reduced the particle size improving the Na^+ diffusion length. The TEM image of $Na_{1.5}Fe_{0.5}Ti_{1.5}(PO_4)_3/C$ shows light-gray zones at the surface of the particles (Fig. 6b) that were not observed for $Na_{1.5}Fe_{0.5}Ti_{1.5}(PO_4)_3$ (Fig. 6a) and can be assigned to carbon. The amount of carbon was estimated from TGA to 1.5 wt%. Thus, the sucrose pyrolysis produced carbon coating, which improved the electrical conductivity of the composite and decreased the polarization. The BET specific area of $Na_{1.5}Fe_{0.5}Ti_{1.5}(PO_4)_3$ and $Na_{1.5}Fe_{0.5}Ti_{1.5}(PO_4)_3/C$ are $0.17 \text{ m}^2 \text{ g}^{-1}$ and $20 \text{ m}^2 \text{ g}^{-1}$, respectively. This strong increase of the specific area by two orders of magnitude confirms the high porosity of the secondary particles

of the composite that is expected to improve electrolyte impregnation and diffusion of Na⁺ ions.

The Raman spectrum of Na_{1.5}Fe_{0.5}Ti_{1.5}(PO₄)₃ (Fig. 7) is similar to those of LiTi₂(PO₄)₃ and NaTi₂(PO₄)₃ with rather close frequencies [25, 55-59]. Based on previously published analyses, all the structures of the present Raman spectrum can be attributed to the NASICON material. The broad band around 1000 cm⁻¹ and the small peak at 1093 cm⁻¹ can be assigned to intramolecular stretching modes of PO₄: the symmetric modes (ν_1) can be assigned to the 962 cm⁻¹ and 985 cm⁻¹ frequencies and the antisymmetric modes (ν_3) to the 1005 cm⁻¹ and 1093 cm⁻¹ frequencies. The small structures in the 500-700 cm⁻¹ range and the sharp peak at 436 cm⁻¹ arise from antisymmetric (ν_4) and symmetric (ν_2) bending modes of PO₄, respectively. The structures below 400 cm⁻¹ are due to external modes and reflect mixtures of different atomic motions. However, it is possible to attribute the main contributions that are due to translational and rotational modes of PO₄ at 336, 310, 225, 195 and 157 cm⁻¹ and to translational modes of Ti⁴⁺/Fe³⁺ at 272 and 225 cm⁻¹. It is worth noting that frequencies in the range 300-400 cm⁻¹ are sensitive to metal substitution such as the Fe substitution for Ti in the octahedral environment [60]. Compared to NaTi₂(PO₄)₃, some small shifts (< 10 cm⁻¹) were observed that can be explained by the difference between the atomic masses of Fe and Ti. In addition, the peaks are overall broadened as expected from the chemical disorder on the 12c crystallographic site that is responsible of bond length and bond angle distributions in both MO₆ (M = Fe, Ti) and PO₄ units as discussed above from DFT calculations (Table 3). Similar effects were observed previously for other cation substituted NASICON compounds [55, 61]. The spectrum of Na_{1.5}Fe_{0.5}Ti_{1.5}(PO₄)₃/C is similar except for a broad band at ~1350 cm⁻¹ and a narrower band at ~1580 cm⁻¹ with notably higher intensities than the vibrational modes of the NASICON phase (Fig. 7). There are also some small changes for frequencies higher than about 700 cm⁻¹, mainly due to overlapping with the main broad band at 1350 cm⁻¹. The two bands at 1350 cm⁻¹ and 1580 cm⁻¹ can be assigned to the D and G bands of residual carbon arising from pyrolysis, respectively. Following the approach of Sadezki *et al* [62], these two bands were fitted to 5 peaks attributed to the vibrational modes of crystalline graphite (G), disordered graphite (D1, D2, D4) and amorphous carbon

(D3) (Fig. 7). The frequencies of the peaks D4, D1, D3, G and D2 are 1231 cm^{-1} , 1346 cm^{-1} , 1464 cm^{-1} , 1575 cm^{-1} and 1604 cm^{-1} , respectively, in line with the values reported for different types of disordered carbons with the same fitting procedure. The relative integrated intensities with respect to G are 0.63 (D4), 2.47 (D1), 0.84 (D3) and 0.43 (D2), respectively. There is no clear correlation between these values and structural information [62] but the intensity ratio between $\text{D1} + \text{D4}$ and $\text{G} + \text{D2}$ (~ 2.2) is similar to the values obtained for different carbon blacks [63] and carbon coating onto LiFePO_4 [64, 65], revealing the existence of small crystalline domains. The rather large D1 linewidth (150 cm^{-1}) suggests a lower degree of graphitization than highly graphitic carbon blacks [62, 63] but is comparable to that found for carbon coating on electrode materials [64, 65]. Thus, TEM and Raman spectroscopy confirmed the existence of graphitic carbon at the surface of the $\text{Na}_{1.5}\text{Fe}_{0.5}\text{Ti}_{1.5}(\text{PO}_4)_3$ particles, which is crucial to improve the electronic conductivity of the composite material.

3.3 Insertion mechanisms and electrochemical performances

The potential curve of the first cycle of $\text{Na}_{1.5}\text{Fe}_{0.5}\text{Ti}_{1.5}(\text{PO}_4)_3/\text{C}$ based electrode obtained in galvanostatic mode (C/10) in the range 1.6-3 V vs. Na^+/Na^0 is displayed in Fig. 8a. The first discharge shows a continuous decrease of the potential from 2.6 to 2.2 V in the range 0-0.5 inserted Na/f.u. (Region R1), followed by a “pseudo-plateau” slightly decreasing from 2.2 to 2.1 V in the range 0.5-2 inserted Na/f.u. (Region R2). The specific capacity for the first discharge is 125 mA h g^{-1} , which is close to the theoretical value of 128 mA h g^{-1} . This small difference can be related to the capacity loss due to the 9 at% electrochemically inactive Fe^{2+} . A similar potential curve was obtained for the first charge except for an irreversible capacity loss of about 5 mA h g^{-1} . The incremental capacity curve of the first discharge exhibits a rather broad band at about 2.3 V (labeled A) and a more intense peak at 2.18 V (labeled B) that can be related to the potential variations in R1 and R2, respectively (Fig. 8b). The first charge shows two structures A' and B' similar to A and B, respectively, except for a broadening of the peak A' compared to A that is also observed in the following cycles. There is a voltage shift between B' and B of about 20 mV, which indicates a small potential

polarization of the electrode material due to low internal impedance and reflects the efficiency of carbon coating.

The GITT curve of the first cycle was recorded in the 1.6-2.3 V range. At each insertion stage, a current of C/10 was applied for 1 h and followed by 8 h relaxation period in order to approach equilibrium potential (Fig. 9). This curve confirms the two-step mechanism with a change of the slope around 0.5 inserted Na/f.u. and also indicates that potential in R2 does not strictly form a plateau even at equilibrium. Such a two-step potential shape differs from the voltage profile of $\text{NaTi}_2(\text{PO}_4)_3$ formed by a well-defined plateau due to a two-phase reaction between the pristine material $\text{NaTi}_2(\text{PO}_4)_3$ ($R\bar{3}c$) and $\text{Na}_3\text{Ti}_2(\text{PO}_4)_3$ ($P\bar{1}$) that reflects the $\text{Ti}^{4+}/\text{Ti}^{3+}$ redox couple [15, 16]. Previous studies on $\text{LiTi}_2(\text{PO}_4)_3$ and $\text{Li}_3\text{Fe}_2(\text{PO}_4)_3$ NASICON based electrode materials for Li-ion batteries show that $\text{Ti}^{4+}/\text{Ti}^{3+}$ [15, 18] and $\text{Fe}^{3+}/\text{Fe}^{2+}$ [66] redox couples operate at about 2.5 and 2.8 V vs. Li^+/Li^0 , respectively. From the difference between the redox potentials of Li^+/Li^0 and Na^+/Na^0 (0.33 V) we can expect that $\text{Ti}^{4+}/\text{Ti}^{3+}$ and $\text{Fe}^{3+}/\text{Fe}^{2+}$ redox couples operate at 2.2 and 2.5 V vs. Na^+/Na^0 , respectively. For $\text{Ti}^{4+}/\text{Ti}^{3+}$, the former value is in line with that of the potential plateau observed for $\text{NaTi}_2(\text{PO}_4)_3$. The present study suggests that potential variations for $\text{Na}_{1.5}\text{Fe}_{0.5}\text{Ti}_{1.5}(\text{PO}_4)_3/\text{C}$ in R1 and R2 could be related to $\text{Fe}^{3+}/\text{Fe}^{2+}$ and $\text{Ti}^{4+}/\text{Ti}^{3+}$ redox couples, respectively.

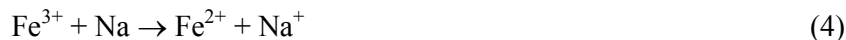
To understand more deeply the effect of the substitution of Fe for Ti on the electrochemical process, we made use of ^{57}Fe Mössbauer spectroscopy during charge-discharge cycles in two different modes. Na insertion was performed in galvanostatic (C/25) and GITT (C/10 and 12 h open-circuit relaxation every 4 h) regimes, respectively, in order to investigate possible kinetic effects and improve the signal-to-noise ratio of the Mössbauer spectra. In galvanostatic regime, the Mössbauer spectra were recorded every 0.08 Na/f.u. during the first cycle in the range 1.6-3 V. All the spectra were fitted with two doublets assigned to Fe^{3+} and Fe^{2+} , respectively. Due to the poor signal-to-noise ratio of the spectra, unexpected randomly large variations of the isomer shift and quadrupole splitting were observed. This is mainly due to the small amount of ^{57}Fe in the sample and the short recording time for each spectrum (4 h). However, it was possible to extract values of the relative areas (RA) of the two components that can be assimilated to the relative amounts of Fe^{3+} and Fe^{2+} .

by assuming they have the same Lamb-Mössbauer factor at room temperature. The variations of these relative amounts vs. number of inserted Na/f.u. show a strong increase of the Fe^{2+} contribution until 80% for 0.5 inserted Na/f.u. followed by some erratic changes in the range 80-95% until the end of discharge (Fig. 10). The inverse trend is obviously obtained for the Fe^{3+} contribution. This mechanism is reversible since the Fe^{2+} amount shows a rather constant trend from the beginning of charge up to about 0.6 inserted Na/f.u. and then strongly decreases until the end of charge. In the GITT experiment, the spectra were recorded every 0.4 Na/f.u. for the first cycle and 0.14 Na/f.u. for half the second discharge. The recording time of 12 h (open-circuit relaxation) was sufficient to extract reliable values of the Mössbauer parameters and sub-spectrum areas. As indicated in the previous section, the Mössbauer spectrum of the pristine $\text{Na}_{1.5}\text{Fe}_{0.5}\text{Ti}_{1.5}(\text{PO}_4)_3/\text{C}$ is formed by two components assigned to Fe^{3+} ($\delta = 0.42 \text{ mm s}^{-1}$, $\Delta = 0.28 \text{ mm s}^{-1}$, RA = 91%) and Fe^{2+} ($\delta = 1.2 \text{ mm s}^{-1}$, $\Delta = 2.4 \text{ mm s}^{-1}$, RA = 9%) originating from high spin Fe^{3+} in crystalline $\text{Na}_{1.5}\text{Fe}_{0.5}\text{Ti}_{1.5}(\text{PO}_4)_3$ and Fe^{2+} impurity, respectively. At the beginning of the first discharge, there is a strong increase of the intensity of a peak at 2.2 mm s^{-1} until the insertion of about 0.8 Na/f.u. (Fig. 11a). More spectra were recorded at the beginning of the second discharge and this peak grows more progressively (Fig. 11c). Through the charge, the spectra change significantly after the extraction of about 1 Na/f.u., showing a decrease of the peak at 2.2 mm s^{-1} until the end of charge (Fig. 11b). All the spectra were fitted with three doublets. One doublet was assigned to Fe^{3+} in $\text{Na}_{1.5}\text{Fe}_{0.5}\text{Ti}_{1.5}(\text{PO}_4)_3$ and the Mössbauer parameters: $\delta = 0.42 \text{ mm s}^{-1}$, $\Delta = 0.28 \text{ mm s}^{-1}$ were kept fixed during the fitting procedure of all the spectra. The second doublet was attributed to Fe^{2+} impurity with the following values: $\delta = 1.2 \text{ mm s}^{-1}$, $\Delta = 2.4 \text{ mm s}^{-1}$, RA = 9% that were also kept fixed. The last doublet was associated to Fe^{2+} arising from the reduction of Fe^{3+} due to Na insertion and its Mössbauer parameters were allowed to vary. In the latter case, only small and insignificant variations of the Mössbauer isomer shift with inserted Na amount were observed that could be assigned to uncertainties arising from the quality of the spectra (Table 6). The average value is $\delta = 1.23 \pm 0.04 \text{ mm s}^{-1}$. The quadrupole splitting exhibits stronger variations that could be related to changes in the local environments of the Fe atoms due to the continuous filling (emptying) of the M2 sites by Na along the

discharge (charge). However, these variations do not exhibit a significant trend, which suggests a random occupation of the M2 sites. The average value is $\Delta = 2.05 \pm 0.12 \text{ mm s}^{-1}$. The value of the isomer shift is close to that found for the Fe^{2+} impurity while the quadrupole splitting is significantly lower. However, these two parameters are both typical of high spin Fe^{2+} . Almost all the Fe^{3+} are transformed into Fe^{2+} at the beginning of the discharge for less than 0.8 Na/f.u and only several percent of Fe^{3+} remained in the second part of the discharge (Fig. 10). This mechanism is reversible since the amount of Fe^{3+} increases only after the extraction of 1 Na/f.u. At the end of charge about 10 at% Fe^{2+} remained in addition to the Fe^{2+} impurity, which proves that sodium extraction was not complete. However, such a value could be due to the specific preparation of the electrode material for Mössbauer measurements as described in the experimental section (powdered sample with only carbon black additive) and the geometry of the *in situ* cell. This explains, for example, the observed maximum amount of 1.6 Na/f.u. inserted Na at the end of the first discharge. During the charge, 1.55 Na/f.u. were extracted and this difference of 0.05 Na/f.u. could affect 10% of the Fe^{2+} atoms within the composite in line with the remaining amount observed by Mössbauer spectroscopy. Finally, the second discharge shows the decrease of the amount of Fe^{3+} for Fe^{2+} , as along the first discharge, but more accurately since more spectra were recorded (Fig. 10). Compared to galvanostatic mode, it is worth noting that GITT mode provided more reliable experimental values of the Mössbauer sub-spectrum areas, as a result of a better signal-to-noise ratio, and larger amounts of Fe^{2+} formed during the discharge probably due to kinetic effects.

For both galvanostatic and GITT regimes, the *operando* Mössbauer spectra clearly show the progressive reduction of Fe^{3+} to Fe^{2+} at the beginning of discharge. In the GITT mode, about 95% of Fe^{3+} was transformed along the discharge until 0.8 inserted Na/f.u., which suggests that the remaining of the discharge is mainly concerned with the Ti^{4+} for Ti^{3+} change. This two-step mechanism, involving first the $\text{Fe}^{3+}/\text{Fe}^{2+}$ change followed by the $\text{Ti}^{4+}/\text{Ti}^{3+}$ reduction, is in line with the electrochemical results and can be related to the peaks A and B of the derivative curve (Fig. 8b). In the same way, the beginning of the charge corresponds to the $\text{Ti}^{3+}/\text{Ti}^{4+}$ oxidation, indicating that the mechanism is reversible. The variations of the relative amounts of Fe^{3+} and Fe^{2+} obtained in galvanostatic and GITT

regimes at the beginning of first or second discharge are quasi-linear and match the expected linear variations for the reaction



Thus, Mössbauer operando experiments provide quantitative evidence that reaction (4) proceeds at the beginning of discharge in all the particles of the composite. This unambiguously proves the one-phase reaction suggested by the shape of the galvanostatic and GITT potential curves. However, it is worth noticing that reaction (4) should be fully completed in $\text{Na}_{1.5}\text{Fe}_{0.5}\text{Ti}_{1.5}(\text{PO}_4)_3/\text{C}$ for 0.5 inserted Na/f.u. which is not exactly the case here since it remains about 10% Fe^{3+} at this step. This amount decreases to 4% for 0.8 inserted Na/f.u. and is then stable until the end of discharge. This suggests the existence of an intermediate mechanism around 0.5 inserted Na/f.u. where both Fe^{3+} and Ti^{4+} are simultaneously reduced.

Electrochemical tests were performed in galvanostatic regime at different current rates. At C/10, the specific capacity after 50 cycles is 119 mAh g⁻¹, which gives a capacity loss from the first discharge of about 5 %, while the coulombic efficiency is 99.8 % (Fig. 12). It is worth noting that coulombic efficiency rapidly increases from 95.6 % to 99 % at the first cycle and then slightly increases up to 99.8 %. This good capacity retention can be related to the good reversibility of the charge-discharge cycles as shown by the stability of both the position and the shape of the peaks A and B of the derivative curves during cycling (Fig. 8b). The rate capability test was performed by 5 cycles at each rate C/10, C/5, C/2, 1C, 2C and 5C, to return to the same rates 2C, 1C, C/2, C/5 and C/10 (Fig. 13). The material delivers specific capacities of 123, 120, 116, 110, 105 and 91 mAh g⁻¹ for C/10, C/5, C/2, 1C, 2C and 5C, respectively, and returns to the initial capacity. Thus, the reversible capacity decreases slightly with increasing discharge rate: the specific capacity at 5C is only 24 % lower than that at C/10, and a good recovery of the initial capacity was obtained. These performances are better than those of $\text{NaTi}_2(\text{PO}_4)_3/\text{C}$ obtained in the present work with the same synthesis procedure especially in terms of capacity retention and power rate. Such improvements were also observed for $\text{Na}_{1+x}\text{Fe}_x\text{Ti}_{2-x}(\text{PO}_4)_3/\text{C}$ nanoparticles obtained by sol-gel method [28]. The positive effect of carbon coating on the electrochemical performances was observed in the

present work from the comparison with $\text{Na}_{1.5}\text{Fe}_{0.5}\text{Ti}_{1.5}(\text{PO}_4)_3$ and $\text{NaTi}_2(\text{PO}_4)_3$ which both show capacity fade and poor power rate. This is due to the low electronic conductivity of the NASICON uncoated materials as previously reported for $\text{NaTi}_2(\text{PO}_4)_3$ [16, 19, 21]. Finally, it is worth noting that high capacity retention and power rate were previously reported for aqueous Na-ion batteries with $\text{NaTi}_2(\text{PO}_4)_3/\text{C}$ as anode [20, 21, 23] and it would be interesting to test the present composition $\text{Na}_{1.5}\text{Fe}_{0.5}\text{Ti}_{1.5}(\text{PO}_4)_3/\text{C}$ in such electrochemical systems.

The present results show that electrochemical insertion of Na in $\text{Na}_{1.5}\text{Fe}_{0.5}\text{Ti}_{1.5}(\text{PO}_4)_3/\text{C}$ follows a two-step mechanism involving successively the $\text{Fe}^{3+}/\text{Fe}^{2+}$ and $\text{Ti}^{4+}/\text{Ti}^{3+}$ transformations in the regions R1 and R2 of the potential curves, respectively. These transformations are reversible during the charge and were observed in both galvanostatic and GITT regimes. This mechanism is in line with the recent results of Aragón *et al* [28] but neither local orderings in R1, nor a clear two-phase reaction in R2 were observed. In addition, these authors observed from *ex situ* Mössbauer spectroscopy that about 20 at% of Fe^{3+} still occur for 1 inserted Na/f.u. at C/20 and disappear at the end of discharge. They proposed that such progressive $\text{Fe}^{3+}/\text{Fe}^{2+}$ transformation along the discharge could be due by kinetic limitations. However, this effect was not observed from our *in situ* Mössbauer experiment in GITT mode conducted at C/10 since only 4 % of Fe^{3+} was detected for 0.8 inserted Na/f.u. These observed discrepancies could be related to differences in the morphology and particle size of the samples obtained by solid-state reaction in the present work and by sol-gel method by Aragón *et al* [28]. The present two-step mechanism also differs from the one-phase reaction previously observed for $\text{Na}_2\text{FeTi}(\text{PO}_4)_3$ [27]. This suggests that increasing x from 0 to 1 in $\text{Na}_{1+x}\text{Fe}_x\text{Ti}_{2-x}(\text{PO}_4)_3$ modifies the insertion mechanism from a two-phase reaction for x=0 to a one-phase reaction for x=1 involving a more complex mechanism for intermediate compositions as shown in the present work. This could be related to changes with x of the electronic structure at the bottom of the conduction band arising from variations in the relative amounts of Fe and Ti. But this could also be attributed to the increasing occupation of the M2 interstitial sites by Na with increasing x that is expected to modify the ionic conductivity.

4. Conclusion

A NASICON based composite with composition $\text{Na}_{1.5}\text{Fe}_{0.5}\text{Ti}_{1.5}(\text{PO}_4)_3/\text{C}$ was synthesized by solid-state route and sucrose pyrolysis. The structural and electrochemical properties of this material were analyzed by combining theoretical and experimental methods. The present study has addressed the effect of the substitution of Fe for Ti in $\text{NaTi}_2(\text{PO}_4)_3/\text{C}$ on the electrochemical performances and insertion mechanisms. The most stable phase predicted by DFT calculations shows that the 3 Na of the rhombohedral primitive cell are located on the two M1 sites and on one M2 site close to Fe. The PBESOL functional provides an excellent agreement between theoretical and experimental structural parameters with accuracy better than 1% on cell volume. This made it possible to describe the different local environments of the two metals that cannot be obtained from XRD and to explain the observed differences with $\text{NaTi}_2(\text{PO}_4)_3$. Both Mössbauer spectroscopy and magnetic measurements showed the existence of high spin Fe^{3+} in $\text{Na}_{1.5}\text{Fe}_{0.5}\text{Ti}_{1.5}(\text{PO}_4)_3$. This is in agreement with DFT calculations, which have additionally confirmed the present experimental value of the Fe quadrupole splitting. The sucrose pyrolysis gave rise to porosity, increasing the BET surface area by two orders of magnitude, and carbon coating. This improved electrolyte impregnation and electronic conductivity and decreases ionic diffusion length. As a consequence, good electrochemical performances were observed for the material used as electrode at 2.2 V vs. Na^+/Na^0 with a stable specific capacity of 120 mA h g^{-1} at C/10, a coulombic efficiency better than 99.5 % and rather high power rate since the capacity loss is 14% at 2C and 24% at 5C. The performances can also be related to the low internal impedance leading to a low potential polarization for the charge-discharge cycles. The substitution of Fe for Ti produces more complex insertion mechanisms than the two-phase and one-phase mechanisms observed for $\text{NaTi}_2(\text{PO}_4)_3$ and $\text{Na}_3\text{Fe}_2(\text{PO}_4)_3$, respectively. ^{57}Fe Mössbauer spectroscopy used in operando mode quantitatively shows linear variations of the Fe^{3+} and Fe^{2+} amounts in $\text{Na}_{1.5}\text{Fe}_{0.5}\text{Ti}_{1.5}(\text{PO}_4)_3/\text{C}$ at the beginning of discharge and at the end of charge for less than about 0.5 inserted Na/f.u. in line with one-phase mechanism suggested by the potential profiles.

ACKNOWLEDGEMENT

Financial supports by Campus France (PHC Toubkal 008/SM/13), the Centre National de la Recherche Scientifique (CNRS, France), the Centre National de la Recherche Scientifique et Technique (CNRST, Maroc), the Swedish Research Council (contract 2012-3392) and StandUp for Energy (Sweden) are gratefully acknowledged. This work was granted access to the HPC resources of CINES under the allocation c2014099131 made by GENCI (CINES, France) for providing computational resources. The authors are grateful to Ali Darwiche, Bernard Fraisse and Corine Reibel from ICG, Montpellier (France) for their assistances in electrochemical cell fabrication, XRD measurements and magnetic measurements, respectively.

1
2
3
4
5
6
REFERENCES

- 7 (1) Ibrahim, H.; Ilinca, A.; Perron, J. Energy Storage Systems-Characteristics and Comparisons.
8 *Renew. Sust. Energ. Rev.* **2008**, *12*, 1221-1250.
- 9 (2) Armand, M.; Tarascon, J.M. Building Better Batteries. *Nature*. **2008**, *451*, 652-657.
- 10 (3) Wadia, C.; Albertus, P.; Srinivasan, V. Resource Constraints on the Battery Energy Storage
11 Potential for Grid and Transportation Applications. *J. Power Sources*. **2011**, *196*, 1593-1598.
- 12 (4) Pan, H.; Hu, Y.S.; Chen, L. Room-Temperature Stationary Sodium-Ion Batteries for Large-Scale
13 Electric Energy Storage. *Energy Environ. Sci.* **2013**, *6*, 2338-2360.
- 14 (5) Kim, H.; Hong, J.; Park, K.Y.; Kim, H.; Kim, S.W. Aqueous Rechargeable Li and Na Ion
15 Batteries. *Chem. Rev.* **2014**, *114*, 11788-11827.
- 16 (6) Yabuuchi, N.; Kubota, K.; Dahbi, M.; Komaba, S. Research Development on Sodium-Ion
17 Batteries. *Chem. Rev.* **2014**, *114*, 11636-11682.
- 18 (7) Dahbi, M.; Yabuuchi, N.; Kubota, K.; Tokiwa, K.; Komaba, S. Negative Electrodes for Na-ion
19 Batteries. *Phys. Chem. Chem. Phys.* **2014**, *16*, 15007-15028.
- 20 (8) Kim, S.W.; Seo, D.H.; Ma, X.; Ceder, G.; Kang, K. Electrode Materials for Rechargeable Sodium-
21 Ion Batteries: Potential Alternatives to Current Lithium-Ion Batteries. *Adv. Energy Mater.* **2012**, *2*,
22 710-721.
- 23 (9) Xu, J.; Lee, D.H.; Meng, Y.S. Room-Temperature Stationary Sodium-Ion Batteries for
24 Large-Scale Electric Energy Storage. *Funct. Mater. Lett.* **2013**, *6*, 1330001-1 - 1330001-7.
- 25 (10) Braconnier, J.; Delmas, C.; Haguenmuller, P. Etude par Désintercalation Electrochimique des
26 Systèmes Na_xCrO_2 et Na_xNiO_2 . *Mater. Res. Bull.* **1982**, *17*, 993-1000.
- 27 (11) Doubaji, S.; Valvo, M.; Saadoune, I.; Dahbi, M.; Edström, K. Synthesis and Characterization of a
28 New Layered Cathode Material for Sodium Ion Batteries. *J. Power Sources*. **2014**, *266*, 275-281.
- 29
30
31
32
33
34
35
36
37
38
39
40
41
42
43
44
45
46
47
48
49
50
51
52
53
54
55
56
57
58
59
60

- (12) Masquelier, C.; Groguec, L. Polyanionic (Phosphates, Silicates, Sulfates) Frameworks as Electrode Materials for Rechargeable Li (or Na) Batteries. *Chem. Rev.* **2013**, *113*, 6552-6591.
- (13) Goodenough, J.B.; Hong, H.Y.P.; Kafalas, J.A. Fast Na^+ -Ion Transport in Skeleton Structures. *Mater. Res. Bull.* **1976**, *11*, 203-220.
- (14) Padhi, A.K.; Nanjundaswamy, K.S.; Goodenough, J.B. Phospho-Olivines as Positive-Electrode Materials for Rechargeable Lithium Batteries. *J. Electrochem. Soc.* **1997**, *144*, 1188-1194.
- (15) Delmas, C.; Cherkaoui, F.; Nadiri, A.; Hagenmuller, P. A Nasicon-Type Phase as Intercalation Electrode: $\text{NaTi}_2(\text{PO}_4)_3$. *Mater. Res. Bull.* **1987**, *22*, 631-639.
- (16) Senguttuvan, P.; Rousse, G.; Arroyo y de Dompablo, M.E.; Vezin, H.; Tarascon, J.M.; Palacin, M.R. Low-Potential Sodium Insertion in a NASICON-Type Structure through the Ti(III)/Ti(II) Redox Couple. *J. Am. Chem. Soc.* **2013**, *135*, 3897-3903.
- (17) Kabbour, H.; Colliot, D.; Colmont, M.; Masquelier, C.; Mentré, O. $\alpha\text{-Na}_3\text{M}_2(\text{PO}_4)_3$ ($\text{M} = \text{Ti, Fe}$): Absolute Cationic Ordering in NASICON-Type Phases. *J. Am. Chem. Soc.* **2011**, *133*, 11900-11903.
- (18) Delmas, C.; Nadiri, A.; Soubeyroux, J.L. The NASICON-Type Titanium Phosphates $\text{ATi}_2(\text{PO}_4)_3$ ($\text{A} = \text{Li, Na}$) as Electrode Materials. *Solid State Ionics*. **1988**, *28-30*, 419.
- (19) Li, Z.; Young, D.; Xiang, K.; Carter, W.C.; Chiang, Y.M. Towards High Power High Energy Aqueous Sodium-Ion Batteries: The $\text{NaTi}_2(\text{PO}_4)_3/\text{Na}_{0.44}\text{MnO}_2$ System. *Adv. Energy Mater.* **2013**, *3*, 290-294.
- (20) Wu, X.; Cao, Y.; Ai, X.; Qian, J.; Yang, H. A Low-Cost and Environmentally Benign Aqueous Rechargeable Sodium-Ion Battery Based on $\text{NaTi}_2(\text{PO}_4)_3-\text{Na}_2\text{NiFe}(\text{CN})_6$ Intercalation Chemistry. *Electrochim. Commun.* **2013**, *31*, 145-148.
- (21) Pang, G.; Nie, P.; Yuan, C.; Shen, L.; Zhang, X.; Li, H.; Zhang, Mesoporous $\text{NaTi}_2(\text{PO}_4)_3/\text{CMK-3}$ Nanohybrid as Anode for Long-Life Na-ion Batteries. *C. J. Mater. Chem. A*. **2014**, *2*, 20659-20666.
- (22) Pang, G.; Yuan, C.; Nie, P.; Ding, B.; Zhu, J.; Zhang, X. Synthesis of NASICON-Type Structured

- 1
2
3 NaTi₂(PO₄)₃-Graphene Nanocomposite as an Anode for Aqueous Rechargeable Na-ion Batteries.
4
5 *Nanoscale*. **2014**, *6*, 6328-6334.
6
7
8 (23) Hou, Z.; Li, X.; Liang, J.; Zhu, Y.; Qian, Y. An Aqueous Rechargeable Sodium Ion Battery
9 Based on a NaMnO₂-NaTi₂(PO₄)₃ Hybrid System for Stationary Energy Storage. *J. Mater. Chem. A*.
10
11 **2015**, *3*, 1400-1404.
12
13
14 (24) Yong, Y.; Wenqin, P. Hydrothermal Synthesis of MTi₂(PO₄)₃ (M = Li, Na, K). *Mater. Res. Bull.*
15
16 **1990**, *25*, 841-844.
17
18
19 (25) Guler, H.; Kurtulus, F. A Rapid Synthesis of Sodium Titanium Phosphate, NaTi₂(PO₄)₃ by Using
20 Microwave Energy. *Mater. Chem. Phys.* **2006**, *99*, 394-397.
21
22
23 (26) Tillement, O.; Angenault, J.; Couturier, J.C.; Quarton, M. Electrochemical Studies of Mixed
24 Valence NASICON. *Solid State Ionics*. **1992**, *53-56*, 391.
25
26
27
28 (27) Patoux, S.; Rousse, G.; Leriche, J.B.; Masquelier, C. Structural and Electrochemical Studies of
29 Rhombohedral Na₂TiM(PO₄)₃ and Li_{1.6}Na_{0.4}TiM(PO₄)₃ (M = Fe, Cr) Phosphates. *Chem. Mater.* **2003**,
30
31 *15*, 2084-2093.
32
33
34 (28) Aragon, M.J.; Vidal-Abarca, C.; Lavela, P.; Tirado, J.L. High Reversible Sodium Insertion into
35 Iron Substituted Na_{1+x}Ti_{2-x}Fe_x(PO₄)₃. *J. Power Sources*. **2014**, *252*, 208-213.
36
37
38 (29) Lippens, P.E.; El Khalifi, M.; Chamas, M.; Perea, A.; Sougrati, M.T.; Ionica-Bousquet, C.; Aldon,
39 L.; Olivier-Fourcade, J.; Jumas, J.C. How Mössbauer Spectroscopy can Improve Li-ion Batteries.
40
41
42
43 *Hyperfine Interact.* **2012**, *206*, 35-46.
44
45
46 (30) Chamas, M.; Sougrati, M.T.; Reibel, C.; Lippens P.E. Quantitative Analysis of the Initial
47 Restructuring step of Nanostructured FeSn₂-Based Anodes for Li-ion Batteries. *Chem. Mater.* **2013**,
48
49 *25*, 2410-2420.
50
51
52 (31) Rietveld, H.M. A profile Refinement Method for Nuclear and Magnetic Structures. *J. Appl.*
53
54 *Crystallogr.* **1969**, *2*, 65-71.
55
56
57
58
59
60

- (32) Rodriguez-Carvajal, J. Recent Advances in Magnetic Structure Determination by Neutron Powder Diffraction + FullProf. *J. Physica B.* **1993**, *192*, 55-56.
- (33) Leriche, J.B.; Hamelet, S.; Shu, J.; Morcrette, M.; Masquelier, C.; Ouvrard, G.; Zerrouki, M.; Soudan, P.; Belin, S.; Elkaïm, E.; Baudelet, F. An Electrochemical Cell for Operando Study of Lithium Batteries Using Synchrotron Radiation. *J. Electrochem. Soc.* **2010**, *157*, A606-610.
- (34) Segall, M.D.; Lindan, P.L.D.; Probert, M.J.; Pickard, C.J.; Hasnip, P.J.; Clark, S.J.; Payne, M.C. First-Principles Simulation: Ideas, Illustrations and the CASTEP Code. *J. Phys.: Condens. Matter.* **2002**, *14*, 2717-2744.
- (35) Kohn, W.; Sham, L.J. Self-Consistent Equations Including Exchange and Correlation Effects. *Phys. Rev.* **1965**, *140*, A1133-1138.
- (36) Hohenberg, P. et Kohn, W. Inhomogeneous Electron Gas. *Phys. Rev. B.* **1964**, *136*, B864-871.
- (37) Perdew, J.P.; Ruzsinszky, A.; Csonka, G.I.; Vydrov, O.A.; Scuseria, G.E.; Constantin, L.A.; Zhou, X.; Burke K. Restoring the Density-Gradient Expansion for Exchange in Solids and Surfaces. *Phys. Rev. Lett.* **2008**, *100*, 136406-1 – 136406-4.
- (38) Vanderbilt, D. Soft Self-Consistent Pseudopotentials in a Generalized Eigenvalue Formalism. *Phys. Rev. B.* **1990**, *42*, 7892-7895.
- (39) Blaha, P.; Schwarz, K.; Madsen, G.K.H; Kvasnicka, D.; J. Luitz, J. WIEN2K An Augmented Plane Wave Plus Local Orbitals Program for Calculating Crystal Properties, Vienna University of Technology, Vienna. **2001**.
- (40) Hagman, L.O.; Kiergaard, P. The crystal Structure of $\text{NaMe}_2^{\text{IV}}(\text{PO}_4)_3$; $\text{Me}^{\text{IV}} = \text{Ge}, \text{Ti}, \text{Zr}$. *Acta Chem. Scand.* **1968**, *22*, 1822-1832.
- (41) Rodrigo, J.L.; Carrasco, P.; Alamo, J. Thermal Expansion of $\text{NaTi}_2(\text{PO}_4)_3$ Studied by Rietveld Method from X-ray Diffraction Data. *Mater. Res. Bull.* **1989**, *24*, 611-618.
- (42) Perdew, J.P.; Burke, K.; Ernzerhof, M. Generalized Gradient Approximation Made Simple. *Phys. Rev. Lett.* **1996**, *77*, 3865-3868.

- (43) Perdew, J.P.; Zunger, A. Self-Interaction Correction to Density-Functional Approximations for Many-Electron Systems. *Phys. Rev. B.* **1981**, *23*, 5048-5079.
- (44) Lajmi, B.; Hidouri, M.; Ben Hammouda, A.; Wattiaux, A.; Fournés, L.; Darriet, J.; Ben Amara, M. Synthesis and Structural Study of a New Iron Phosphate $K_3Fe(PO_4)_2$. *Mater. Chem. Phys.* **2009**, *113*, 372-375.
- (45) Jirack, Z.; Salmon, R.; Fournés, L.; Menil, F.; Haguenmuller, P. Magnetic and Mössbauer Resonance Investigations of the Weak Ferrimagnet Iron Molybdate $(Fe_2(MoO_4)_3)$. *Inorg. Chem.* **1982**, *21*, 4218-4223.
- (46) Beltran-Porter, D.; Olazcuaga, R.; Fournes, L.; Menil, F.; Le Flem, G. Etude Magnétique et par Résonance Mössbauer de l'Orthophosphate $Na_3Fe_2(PO_4)_3\alpha$ et d'une Phase Vitreuse Dérivée. *Revue Phys. Appl.* **1980**, *15*, 1155-1160.
- (47) Blaha, P.; Schwarz, K.; Herzig, P. First-Principles Calculation of the Electric Field Gradient of Li_3N . *Phys. Rev. Lett.* **1985**, *54*, 1192-1195.
- (48) Lippens, P.E.; Olivier-Fourcade, J.; Jumas, J.C. Interpretation of the ^{119}Sn Mössbauer parameters. *Hyperfine Interact.* **2000**, *126*, 137-141.
- (49) Lippens, P.E.; Jumas, J.C.; Olivier-Fourcade, J. Calculation of ^{121}Sb and ^{125}Te Mössbauer Spectra. *Hyperfine Interact.* **2002**, *141-142*, 303-308.
- (50) Weibel, A.; Bouchet, R.; Savin, S.L.P.; Chadwick, A.V.; Lippens, P.E.; Womes, M.; Knauth, P. Local Atomic and Electronic Structure in Nanocrystalline Sn-Doped Anatase TiO_2 . *ChemPhysChem*. **2006**, *7*, 2377-2383.
- (51) Yahla, H.; Boukra, A.; Belhakem, M.; Lippens, P.E. First-Principles Calculations of the Electronic Structure and Mössbauer Parameters of Sb-Doped SnO_2 . *Solid State Com.* **2009**, *149*, 2202-2206.
- (52) Dufek, P.; Blaha, P.; Schwarz, K. Determination of the Nuclear Quadrupole Moment of ^{57}Fe . *Phys. Rev. Lett.* **1995**, *75*, 3545-3548.

- (53) Boucher, F.; Gaubicher, J.; Cuisinier, M.; Guyomard, D.; Moreau, P. Elucidation of the $\text{Na}_{2/3}\text{FePO}_4$ and $\text{Li}_{2/3}\text{FePO}_4$ Intermediate Superstructure Revealing a Pseudouniform Ordering in 2D. *J. Am. Chem. Soc.* **2014**, *136*, 9144-9157.
- (54) Greaves, C.; Slater, P.R.; Slaski, M.; Muirhead, C.M. The Nature of Magnetic Ordering at 47 K in $\text{Na}_3\text{Fe}_2(\text{PO}_4)_3$. *Physica B*. **1994**, *194-196*, 199-200.
- (55) Cretin, M.; Fabry, P.; Abello, L. Study of $\text{Li}_{1+x}\text{Al}_x\text{Ti}_{2-x}(\text{PO}_4)_3$ for Li^+ Potentiometric Sensors. *J. European Ceramic Soc.* **1995**, *15*, 1149-1156.
- (56) Burba, C.M.; Frech, R. Vibrational Spectroscopic Study of Lithium Intercalation into $\text{LiTi}_2(\text{PO}_4)_3$. *Solid State Ionics*. **2006**, *177*, 1489-1494.
- (57) Butt, G.; Sammes, N.; Tompsett, G.; Smirnova, A.; Yamamoto, O. Raman Spectroscopy of Superionic Ti-Doped $\text{Li}_3\text{Fe}_2(\text{PO}_4)_3$ and LiNiPO_4 Structures. *J. Power Sources*. **2004**, *134*, 72-79.
- (58) Yong, Y.; Wenqin, P. Hydrothermal Synthesis of $\text{MTi}_2(\text{PO}_4)_3$ ($\text{M} = \text{Li}, \text{Na}, \text{K}$). *Mat. Res. Bull.* **1990**, *25*, 841-844.
- (59) Bamberger, C.E.; Begun, G.M. Synthesis and Characterization of Sodium-Titanium Phosphates, $\text{Na}_4(\text{TiO})(\text{PO}_4)_2$, $\text{Na}(\text{TiO})\text{PO}_4$, and $\text{NaTi}_2(\text{PO}_3)_3$. *J. Solid State Chem.* **1988**, *73*, 317-324.
- (60) Barj, M.; Lucaleau, G.; Delmas, C. Raman and Infrared Spectra of Some Chromium Nasicon-Type Materials: Short-Range Disorder Characterization. *J. Solid State Chem.* **1992**, *100*, 141-150.
- (61) Junaid Bushiri, M.; Antony, C.J.; Aatiq, A. Raman and FTIR Studies of the Structural Aspects of NASICON-Type Crystals; $\text{AFeTi}(\text{PO}_4)_3$ [$\text{A} = \text{Ca}, \text{Cd}$]. *J. Phys. Chem. Solids*. **2008**, *69*, 1985-1989.
- (62) Sadezky, A.; Muckenhuber, H.; Grothe, H.; Niessner, R.; Pöschl, U. Raman Microspectroscopy of Soot and Related Carbonaceous Materials: Spectral Analysis and Structural Information. *Carbon*. **2005**, *43*, 1731-1742.
- (63) Jawhari, T.; Roid, A.; Casado, J. Raman Spectroscopic Characterization of Some Commercially Available Carbon Black Materials. *Carbon*. **1995**, *33*, 1561-1565.

- 1
2
3 (64) Doeuff, M.M.; Hu, Y.; McLarnon, F.; Kostecki, R. Effect of Surface Carbon Structure on the
4
5 Electrochemical Performance of LiFePO₄. *Electrochem. Solid-State Lett.* **2003**, *6*, A207-A209.
6
7
8 (65) Julien, C.M.; Zaghib, K.; Mauger, A.; Massot, M.; Ait-Salah A.; Selmene, M.; Gendron, F.
9 Characterization of the Carbon Coating onto LiFePO₄ Particles Used in Lithium Batteries. *J. Appl.*
10
11 *Phys.* **2006**, *100*, 063511-1 – 063511-7.
12
13
14 (66) Morcrette, M.; Wurm, C.; Masquelier, C. On the Way to the Optimization of Li₃Fe₂(PO₄)₃
15 Positive Electrode Materials. *Solid State Sci.* **2002** (1), *4*, 239-246.
16
17
18
19
20
21
22
23
24
25
26
27
28
29
30
31
32
33
34
35
36
37
38
39
40
41
42
43
44
45
46
47
48
49
50
51
52
53
54
55
56
57
58
59
60

TABLES

Table 1. Theoretical (DFT) and experimental (XRD) values of the structural parameters of NaTi₂(PO₄)₃: lattice parameters (a, c) and atomic coordinates (x, y, z) given in the hexagonal system, rhombohedral unit cell volume (V_{rho}) and interatomic distances (d).

	DFT	XRD
a (Å), c (Å)	8.521, 21.748	8.482(9), 21.794(3)
V_{rho} (Å³)	455.9	452.5
Ti (x,y,z)	0, 0, 0.1442	0, 0, 0.1447
P (x,y,z)	0.2870, 0, 0.25	0.2857, 0.0000, 0.25
O(1) (x,y,z)	0.1754, 0.9803, 0.1928	0.1740, 0.9755, 0.1926
O(2) (x,y,z)	0.1925, 0.1652, 0.0878	0.1910, 0.1661, 0.0884
d(Na-O) (Å)	2.451 x 6	2.457 x 6
d(Ti-O) (Å)	1.906 x 3 + 1.967 x 3	1.902 x 3 + 1.958 x 3
d(P-O) (Å)	1.523 x 2 + 1.524 x 2	1.520 x 2 + 1.528 x 2

1
2
3
4
5
6
7
8
9
10
11
12
13
14
15 **Table 2.** Averaged theoretical values of the structural parameters of the most stable
16 $\text{Na}_{1.5}\text{Fe}_{0.5}\text{Ti}_{1.5}(\text{PO}_4)_3$ phase obtained by DFT calculations: lattice parameters (a, c), atomic positions (x,
17 y, z) given in hexagonal system, rhombohedral unit cell volume (V_{rho}). The expected corresponding
18 general coordinates of the crystallographic sites in $R\bar{3}c$ are given for comparison.
19
20
21
22
23
24
25
26
27

	DFT	Expected crystallographic site
a (Å), c (Å)	8.582, 21.685	
V_{rho} (Å ³)	461.0	
Na(M1)	-0.0103, -0.0079, -0.0013	0, 0, 0 (6b)
Na(M2)	0.6347, 0.0006, 0.2470	x, 0, 1/4 (18e)
M	-0.0012, -0.0002, 0.1458	0, 0, x (12c)
P	0.2884, -0.0004, 0.2508	x, 0, 1/4 (18e)
O(1)	0.1775, 0.9810, 0.1926	x, y, z (36f)
O(2)	0.1921, 0.1663, 0.0874	x, y, z (36f)

Table 3. Theoretical interatomic distances d_i ($i=1,n$ where n is the number of nearest neighbors), average distances d_{av} and polyhedron distance distortions Δ_{poly} obtained from DFT calculations for MO_6 octahedra with $M = Ti$ or Fe ($n=6$), $Na(M1)O_6$ ($n=6$) and $Na(M2)O_8$ ($n=8$) polydra of $Na_{1.5}Fe_{0.5}Ti_{1.5}(PO_4)_3$. The polyhedron distance distortion Δ_{poly} is defined by $\Delta = \frac{1}{n} \sum_{i=1}^n \left(\frac{d_i - d_{av}}{d_{av}} \right)^{1/2}$

	Interatomic distances (Å)						d_{av} (Å)	Δ_{octa}
Ti1-O	1.871	1.872	1.948	1.957	2.025	2.027	1.950	$1.05 \cdot 10^{-3}$
Ti2-O	1.891	1.906	1.914	1.953	1.959	1.961	1.931	$2.08 \cdot 10^{-4}$
Ti3-O	1.905	1.936	1.938	1.951	1.966	1.974	1.945	$1.36 \cdot 10^{-4}$
Fe-O	1.914	1.915	1.993	2.012	2.088	2.089	2.002	$1.27 \cdot 10^{-3}$
Na1-O	2.374	2.388	2.414	2.458	2.555	2.600	2.465	$1.20 \cdot 10^{-3}$
Na2-O	2.343	2.410	2.414	2.427	2.475	2.583	2.442	$9.10 \cdot 10^{-4}$
Na3-O	2.294	2.343	2.374	2.400	2.409	2.532	2.741	2.913
							2.501	$6.63 \cdot 10^{-3}$

1
2 **Table 4.** Structural parameters of $\text{Na}_{1.5}\text{Fe}_{0.5}\text{Ti}_{1.5}(\text{PO}_4)_3$ obtained from Rietveld refinement. The lattice
3 parameters (a , c) and the atomic positions (x , y , z) are given in the hexagonal system while the volume
4 (vol.) is that of the rhombohedral unit cell.
5
6
7

Atom	Site symmetry	x	y	z	Occupation rate	B_{iso} (Å ²)
Na(1)	6b	0.0	0.0	0.0	0.9799(1)	4.627 (1)
Na(2)	18e	0.6376(9)	0.0	¼	0.5200(9)	2.374(1)
Ti(1)	12c	0.0	0.0	0.1439(4)	1.500(1)	2.375(1)
Fe(1)	12c	0.0	0.0	0.1439(4)	0.500(1)	2.375(1)
P(1)	18e	0.2875(9)	0.0	¼	3.000(1)	1.909(1)
O(1)	36f	0.1747(8)	0.9759(1)	0.1926(2)	6.000(1)	0.207(1)
O(2)	36f	0.1979(1)	0.1668(6)	0.0883(4)	6.000(1)	0.281(1)

41 Profile parameters
42
43 X= 0.0029 (1)
44
45 U= 0.04189(3)
46
47 V= -0.02081(1)
48
49 W= 0.01871(6)
50

51 Conventional Rietveld R-factors for points with Bragg contribution
52

53 Rp: 20.1 %; Rwp =19.3 %; R_B= 8.35 %
54

Table 5. ^{57}Fe Mössbauer parameters of $\text{Na}_{1.5}\text{Fe}_{0.5}\text{Ti}_{1.5}(\text{PO}_4)_3$ and $\text{Na}_{1.5}\text{Fe}_{0.5}\text{Ti}_{1.5}(\text{PO}_4)_3/\text{C}$ at room temperature: isomer shift relative to $\alpha\text{-Fe}$ (δ), quadrupole splitting (Δ), linewidth at half maximum (Γ), relative area of the subspectra (RA) and assigned Fe sites.

	δ (mm/s)	Δ (mm/s)	Γ (mm/s)	RA (%)	Site
$\text{Na}_{1.5}\text{Fe}_{0.5}\text{Ti}_{1.5}(\text{PO}_4)_3$	0.437(1)	0.326(2)	0.414(4)	100	$\text{Fe}^{3+}[\text{Oh}]$
$\text{Na}_{1.5}\text{Fe}_{0.5}\text{Ti}_{1.5}(\text{PO}_4)_3/\text{C}$	0.420(7)	0.275(5)	0.400(3)*	91	$\text{Fe}^{3+}[\text{Oh}]$
	1.178(7)	2.368(2)	0.400(3)*	9	$\text{Fe}^{2+}[\text{Oh}]$

*constrained to be equal

Table 6. ^{57}Fe Mössbauer parameters of $\text{Na}_{1.5}\text{Fe}_{0.5}\text{Ti}_{1.5}(\text{PO}_4)_3/\text{C}$ based electrode at different stages of the electrochemical discharge-charge process in *operando* GITT mode (see text for details): isomer shift relative to $\alpha\text{-Fe}$ (δ), quadrupole splitting (Δ), linewidth at half maximum (Γ), relative area of the subspectra (RA) and assigned Fe sites.

First Discharge: number of inserted Na/f.u.	δ (mm/s)	Δ (mm/s)	Γ (mm/s)	RA (%)	Site
0	0.411(4) 1.242(8)	0.341(9) 2.663(4)	0.440(3) 0.440(3)	91 9	$\text{Fe}^{3+}[\text{Oh}]$ $\text{Fe}^{2+}[\text{Oh}]$
0.4	1.233(6) 1.242* 0.411*	1.972(7) 2.663* 0.341*	0.463(2) 0.463(2)** 0.463(2)**	78 9 13	$\text{Fe}^{2+}[\text{Oh}]$ Impurity $\text{Fe}^{3+}[\text{Oh}]$
0.8	1.259(3) 1.242* 0.411*	2.009(3) 2.663* 0.341*	0.487(2) 0.487(2)** 0.487(2)**	87 9 4	$\text{Fe}^{2+}[\text{Oh}]$ Impurity $\text{Fe}^{3+}[\text{Oh}]$
1.2	1.245(4) 1.242* 0.411*	2.001(5) 2.663* 0.341*	0.474(6) 0.474(6)** 0.474(6)**	86 9 5	$\text{Fe}^{2+}[\text{Oh}]$ Impurity $\text{Fe}^{3+}[\text{Oh}]$
1.6 End of discharge	1.258(1) 1.242* 0.411*	2.036(5) 2.663* 0.341*	0.474(6) 0.474(6)** 0.474(6)**	88 9 3	$\text{Fe}^{2+}[\text{Oh}]$ Impurity $\text{Fe}^{3+}[\text{Oh}]$
First Charge : number of extracted Na/f.u.					
0.4	1.234(6) 1.242* 0.411*	1.984(4) 2.663* 0.341*	0.544(5) 0.544(5)** 0.474(6)**	87 9 4	$\text{Fe}^{2+}[\text{Oh}]$ Impurity $\text{Fe}^{3+}[\text{Oh}]$
0.8	1.241(6) 1.242* 0.411*	2.063(1) 2.663* 0.341*	0.479(1) 0.479(1)** 0.479(1)**	86 9 5	$\text{Fe}^{2+}[\text{Oh}]$ Impurity $\text{Fe}^{3+}[\text{Oh}]$
1.2	1.211(4) 1.242* 0.411*	2.025(4) 2.663* 0.341*	0.444(1) 0.444(1)** 0.444(1)**	62 9 29	$\text{Fe}^{2+}[\text{Oh}]$ Impurity $\text{Fe}^{3+}[\text{Oh}]$

	1.56	1.216(1)	2.179(5)	0.479(8)	14	$\text{Fe}^{2+}[\text{Oh}]$
	End of charge	1.242*	2.663*	0.479**	9	Impurity
		0.411*	0.341*	0.479**	77	$\text{Fe}^{3+}[\text{Oh}]$
	Second Discharge: number of inserted Na/f.u.					
	0.14	1.210(1)	1.989(5)	0.498(1)	49	$\text{Fe}^{2+}[\text{Oh}]$
		1.242*	2.663*	0.498(1)**	9	Impurity
		0.411*	0.341*	0.498(1)**	42	$\text{Fe}^{3+}[\text{Oh}]$
	0.28	1.215(6)	2.053(2)	0.428(1)	67	$\text{Fe}^{2+}[\text{Oh}]$
		1.242*	2.663*	0.428(1)**	9	Impurity
		0.411*	0.341*	0.428(1)**	24	$\text{Fe}^{3+}[\text{Oh}]$
	0.42	1.224(9)	2.079(1)	0.501(9)	76	$\text{Fe}^{2+}[\text{Oh}]$
		1.242*	2.663*	0.501(9)**	9	Impurity
		0.411*	0.341*	0.501(9)**	15	$\text{Fe}^{3+}[\text{Oh}]$
	0.56	1.233(1)	2.057(2)	0.425(3)	80	$\text{Fe}^{2+}[\text{Oh}]$
		1.242*	2.663*	0.425(3)**	9	Impurity
		0.411*	0.341*	0.425(3)**	11	$\text{Fe}^{3+}[\text{Oh}]$
	0.7	1.246(2)	2.041(7)	0.460(1)	90.5	$\text{Fe}^{2+}[\text{Oh}]$
		1.242*	2.663*	0.460(1)**	9	Impurity
		0.411*	0.341*	0.460(1)**	0.5	$\text{Fe}^{3+}[\text{Oh}]$

* fixed

** constrained to be equal

Figure captions

Figure 1. Theoretical optimized rhombohedral unit cell of $\text{Na}_{1.5}\text{Fe}_{0.5}\text{Ti}_{1.5}(\text{PO}_4)_3$ with Na(M1) (light green), Na(M2) (green), Fe (red), P(pink), Ti (blue) and O (yellow) (a). The dots indicate the interatomic distances (in Å) between the cations located along the hexagonal axis c_{hex} . Local structure of Fe bonded to 6 O first-nearest neighbors forming a distorted octahedron and the two closest Na in M1 and M2. The interatomic distances (in Å) and the bond angles (in degree) are also shown (b).

Figure 2. XRD patterns of $\text{Na}_{1.5}\text{Fe}_{0.5}\text{Ti}_{1.5}(\text{PO}_4)_3$ (a) and $\text{Na}_{1.5}\text{Fe}_{0.5}\text{Ti}_{1.5}(\text{PO}_4)_3/\text{C}$ (b): experimental data (red circles), Rietveld refinement (black line), Bragg positions (green bars) and difference between experimental data and fitted curve (blue line).

Figure 3. ^{57}Fe Mössbauer spectra of $\text{Na}_{1.5}\text{Fe}_{0.5}\text{Ti}_{1.5}(\text{PO}_4)_3$ (a) and $\text{Na}_{1.5}\text{Fe}_{0.5}\text{Ti}_{1.5}(\text{PO}_4)_3/\text{C}$ (b) at room temperature. In the later case, the Fe^{3+} and Fe^{2+} sub-spectra are plotted in red and green, respectively.

Figure 4. Temperature dependence of the inverse magnetic susceptibility of $\text{Na}_{1.5}\text{Fe}_{0.5}\text{Ti}_{1.5}(\text{PO}_4)_3$ (black dots) and $\text{Na}_{1.5}\text{Fe}_{0.5}\text{Ti}_{1.5}(\text{PO}_4)_3/\text{C}$ (red dots).

Figure 5. SEM images of $\text{Na}_{1.5}\text{Fe}_{0.5}\text{Ti}_{1.5}(\text{PO}_4)_3$ (a) and $\text{Na}_{1.5}\text{Fe}_{0.5}\text{Ti}_{1.5}(\text{PO}_4)_3/\text{C}$ (b).

Figure 6. TEM images of $\text{Na}_{1.5}\text{Fe}_{0.5}\text{Ti}_{1.5}(\text{PO}_4)_3$ (a) and $\text{Na}_{1.5}\text{Fe}_{0.5}\text{Ti}_{1.5}(\text{PO}_4)_3/\text{C}$ (b).

1
2
Figure 7. Raman spectra of $\text{Na}_{1.5}\text{Fe}_{0.5}\text{Ti}_{1.5}(\text{PO}_4)_3$ (black line) and $\text{Na}_{1.5}\text{Fe}_{0.5}\text{Ti}_{1.5}(\text{PO}_4)_3/\text{C}$ (red line).

3
4
Insert: curve fitting of D and G bands.
5
6
7
8
9

10
Figure 8. Galvanostatic voltage curve (C/10, 1.6-3.0 V vs. Na^+/Na^0) for the first cycle of
11
12
13
14
 $\text{Na}_{1.5}\text{Fe}_{0.5}\text{Ti}_{1.5}(\text{PO}_4)_3/\text{C}$ (a) and derivative curves for different numbers of cycles (b). R1 and R2 denote
15
the regions of the two-step insertion mechanism.
16
17
18
19

20
Figure 9. GITT potential curve of the first discharge of $\text{Na}_{1.5}\text{Fe}_{0.5}\text{Ti}_{1.5}(\text{PO}_4)_3/\text{C}$. R1 and R2 denote the
21
22
regions of the two-step insertion mechanism.
23
24
25
26
27

28
Figure 10. Variations of the relative areas of the sub-spectrum of Fe^{3+} (red) and of the sum of the two
29
30 sub-spectra assigned to Fe^{2+} in $\text{Na}_{1.5}\text{Fe}_{0.5}\text{Ti}_{1.5}(\text{PO}_4)_3/\text{C}$ and to Fe^{2+} impurity (blue). The results are
31
32 given for *operando* galvanostatic (circles) and GITT (squares) modes. The solid lines are guides for
33
34 the eye.
35
36
37
38
39

40
Figure 11. Operando ^{57}Fe Mössbauer spectra of $\text{Na}_{1.5}\text{Fe}_{0.5}\text{Ti}_{1.5}(\text{PO}_4)_3/\text{C}$ recorded during the first cycle
41
42 and at the beginning of the second discharge in GITT mode.
43
44
45
46
47

48
Figure 12. Specific capacity and Coulombic efficiency of $\text{Na}_{1.5}\text{Fe}_{0.5}\text{Ti}_{1.5}(\text{PO}_4)_3/\text{C}$ measured in
49
50 galvanostatic mode at C/10 in the range 1.6-3.0 V vs. Na^+/Na^0 .
51
52
53
54
55

56
Figure 13. Rate and cycling performances of $\text{Na}_{1.5}\text{Fe}_{0.5}\text{Ti}_{1.5}(\text{PO}_4)_3/\text{C}$.
57
58
59
60

Figure 1

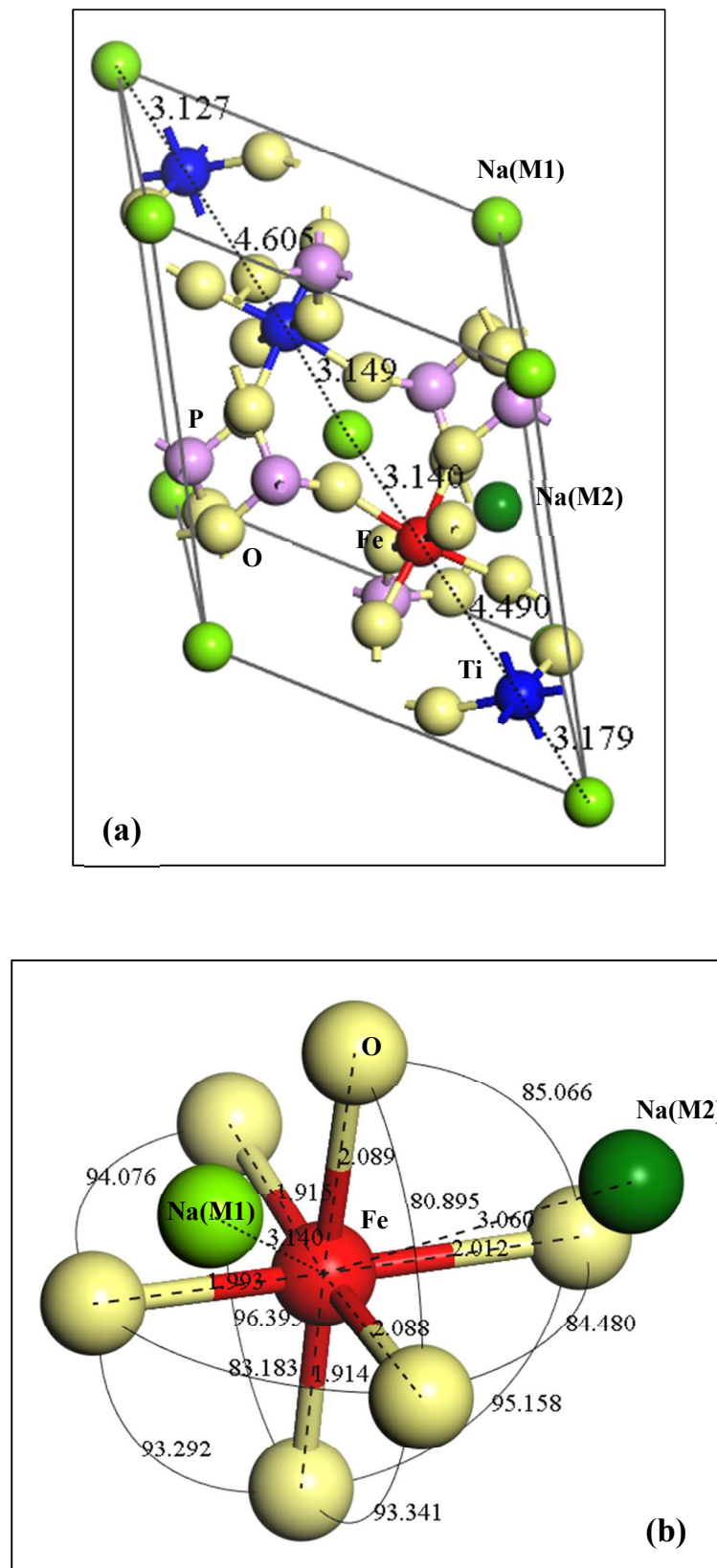


Figure 2

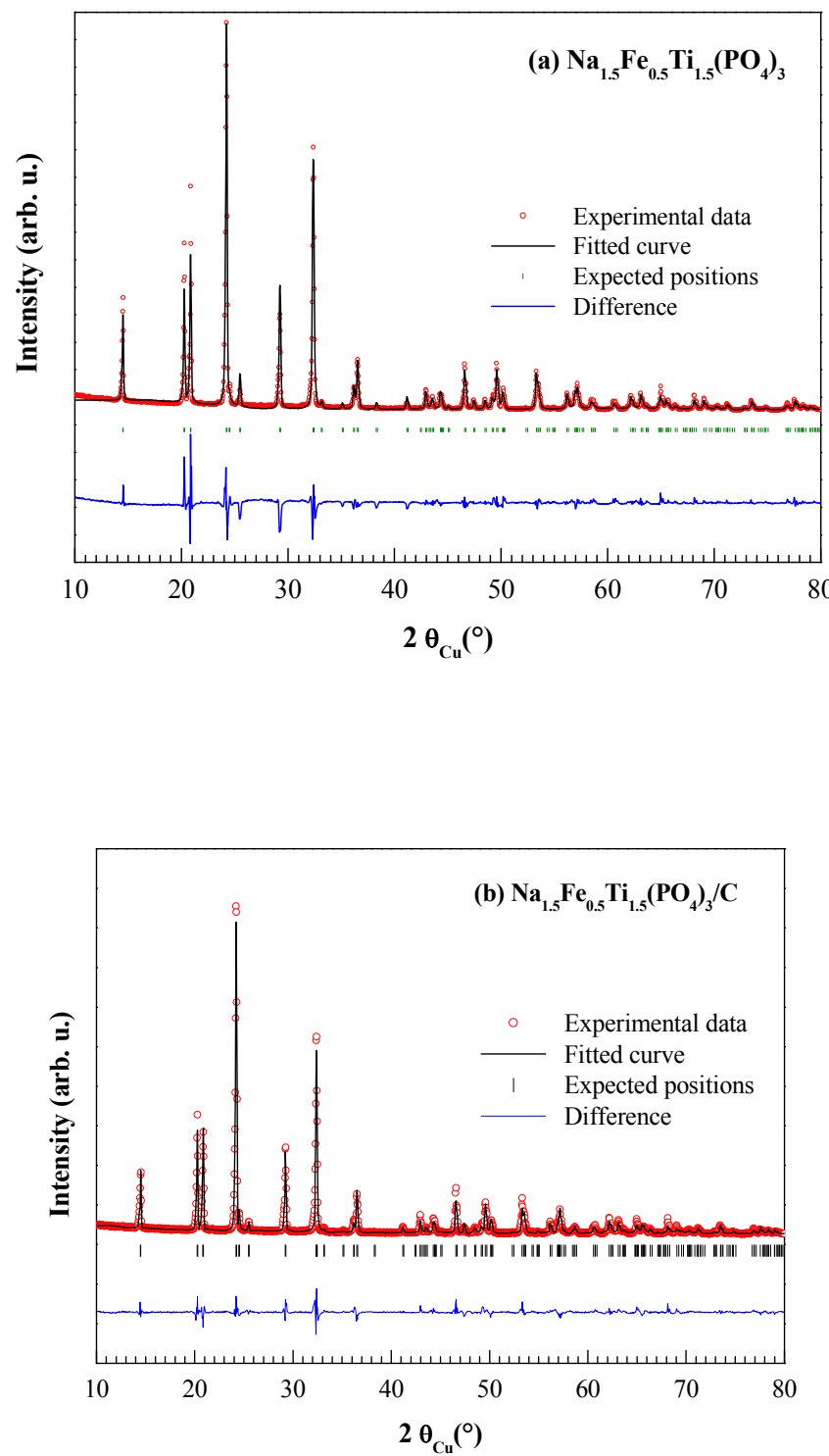


Figure 3

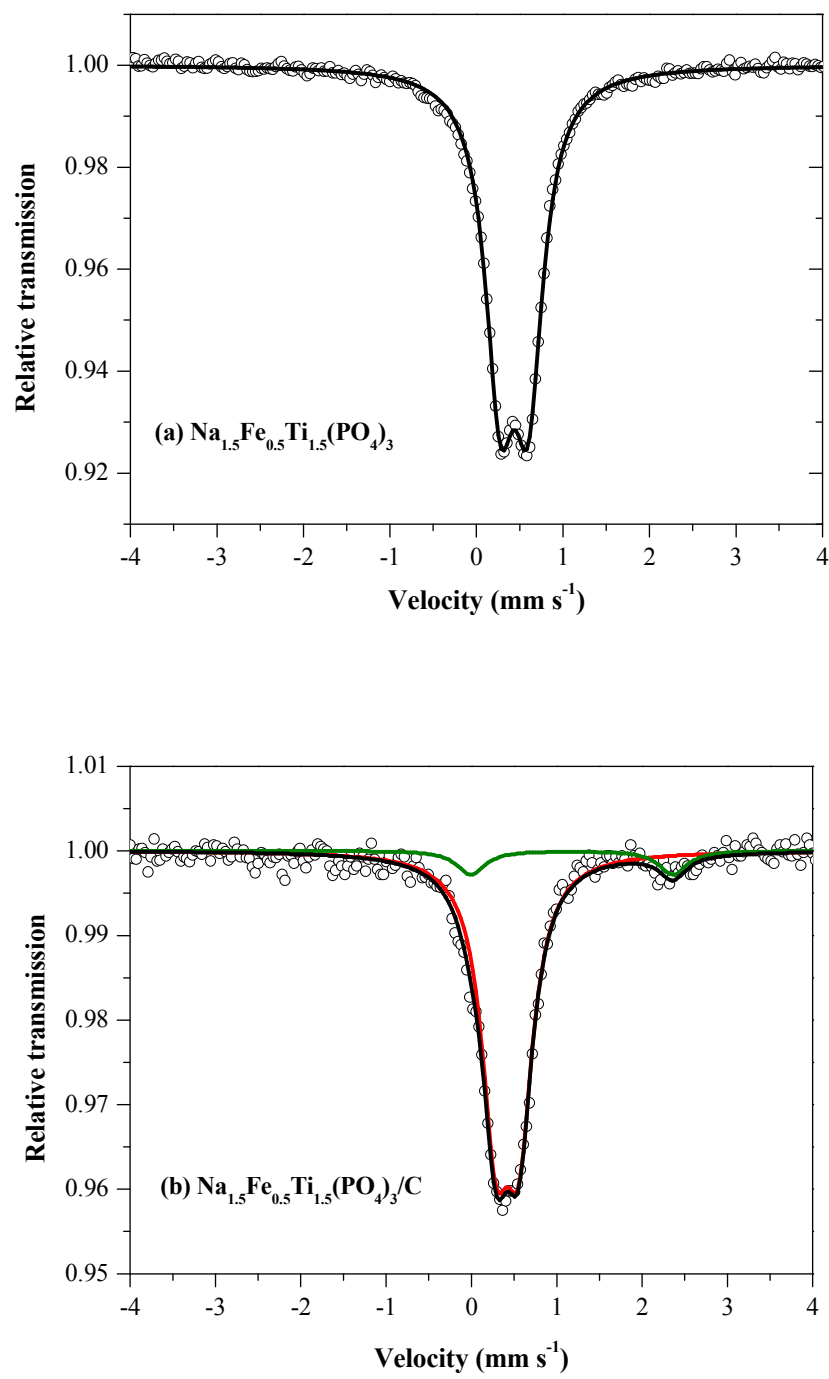
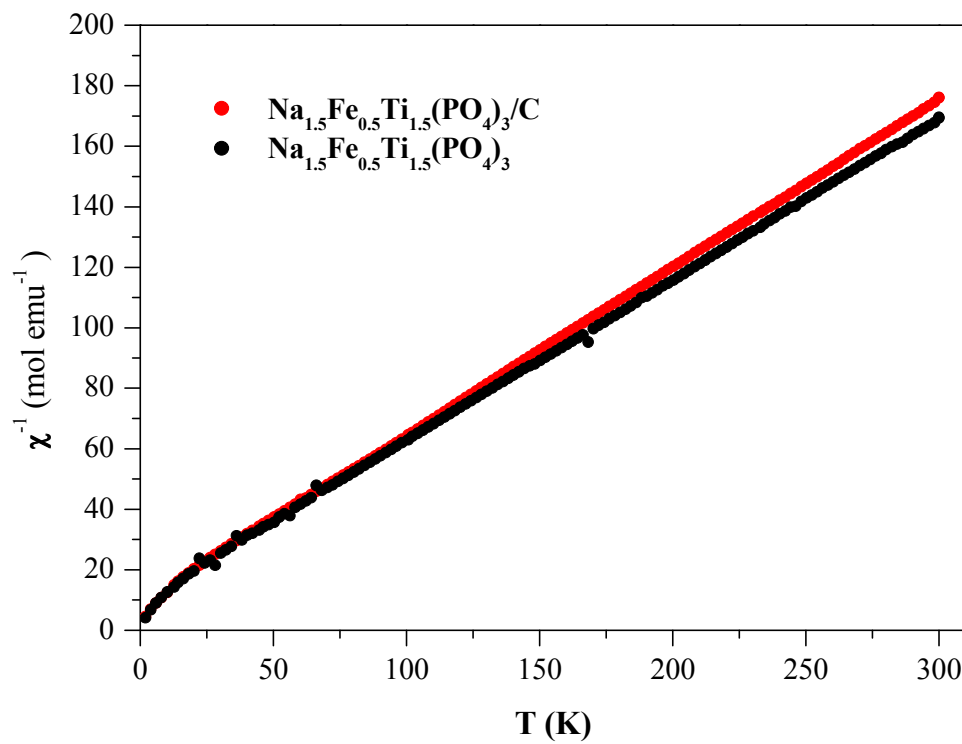


Figure 4



1
2
3 **Figure 5**
4
5
6
7
8
9
10
11
12
13
14
15
16
17
18
19
20
21
22
23
24
25
26
27
28
29
30
31
32
33
34
35
36
37
38

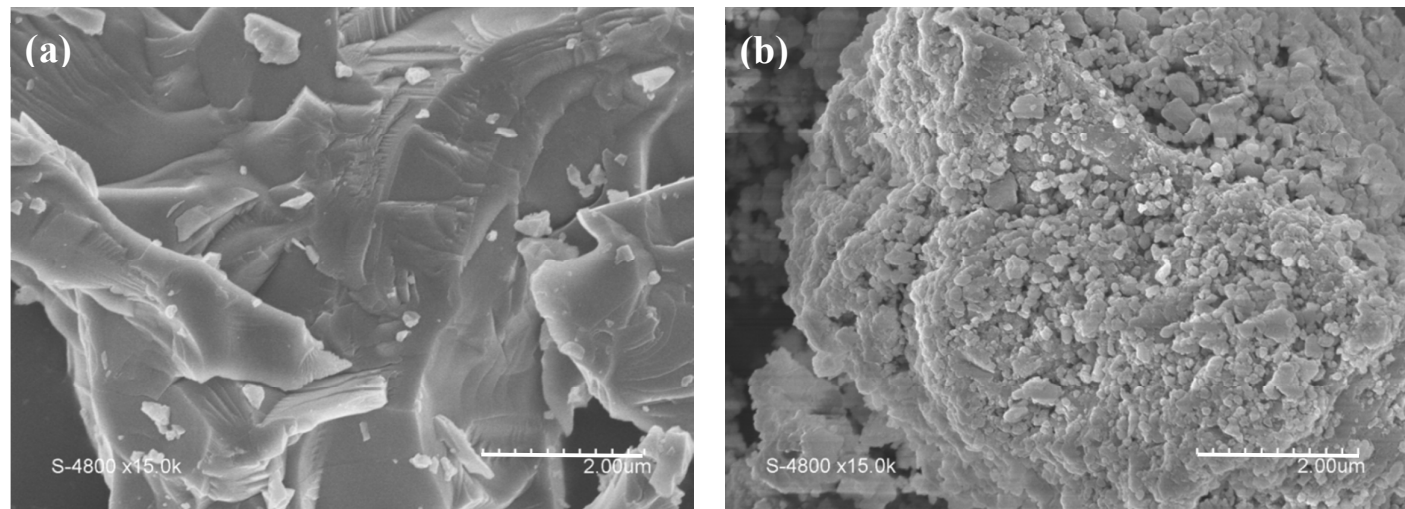


Figure 6

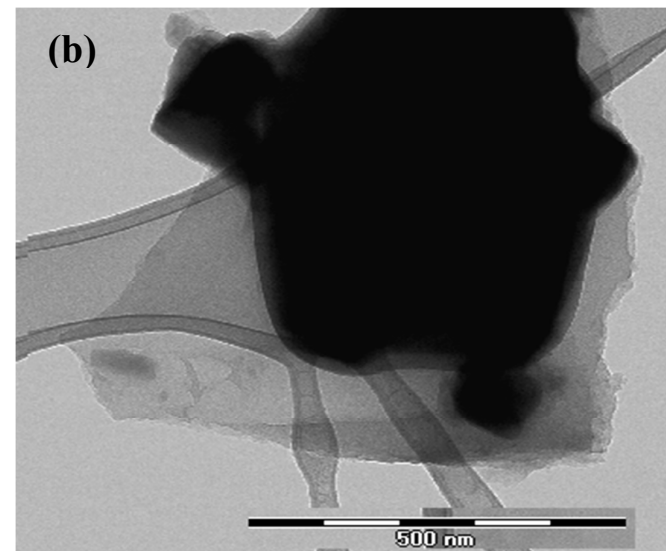
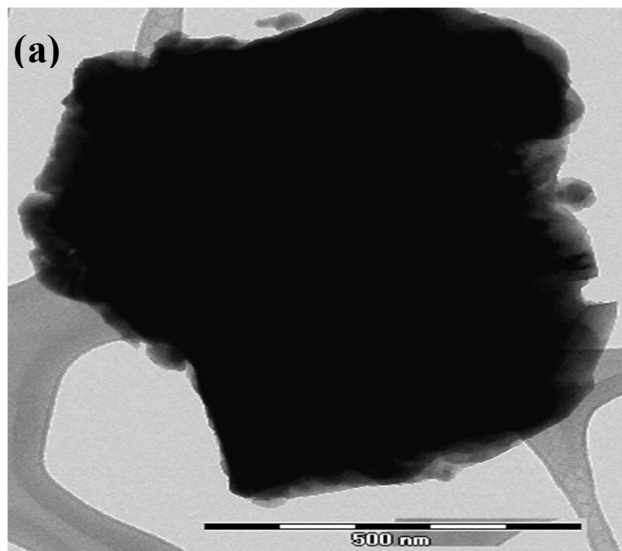


Figure 7

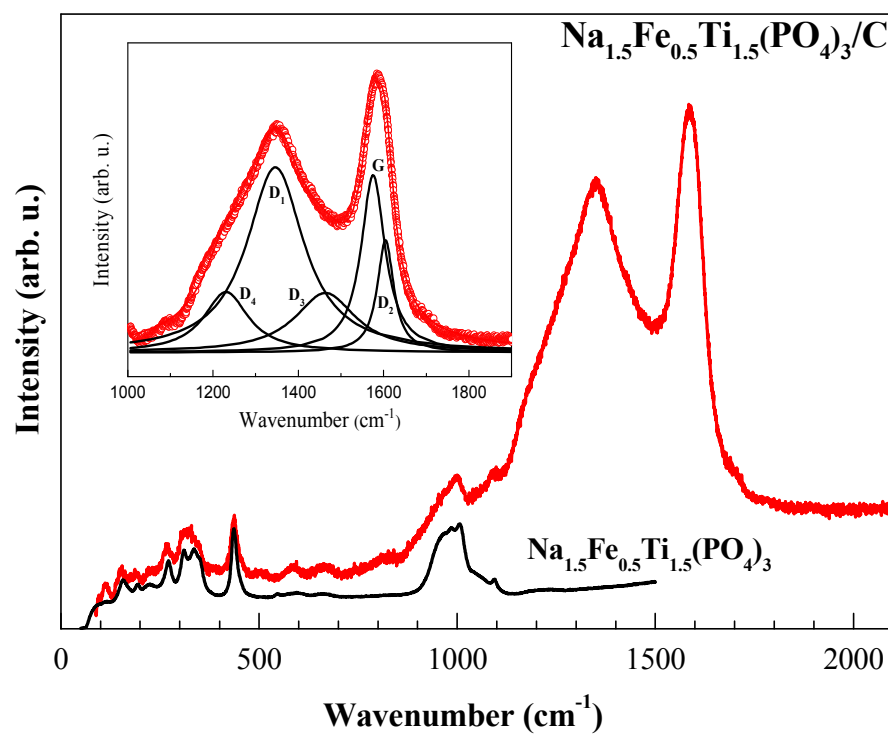


Figure 8

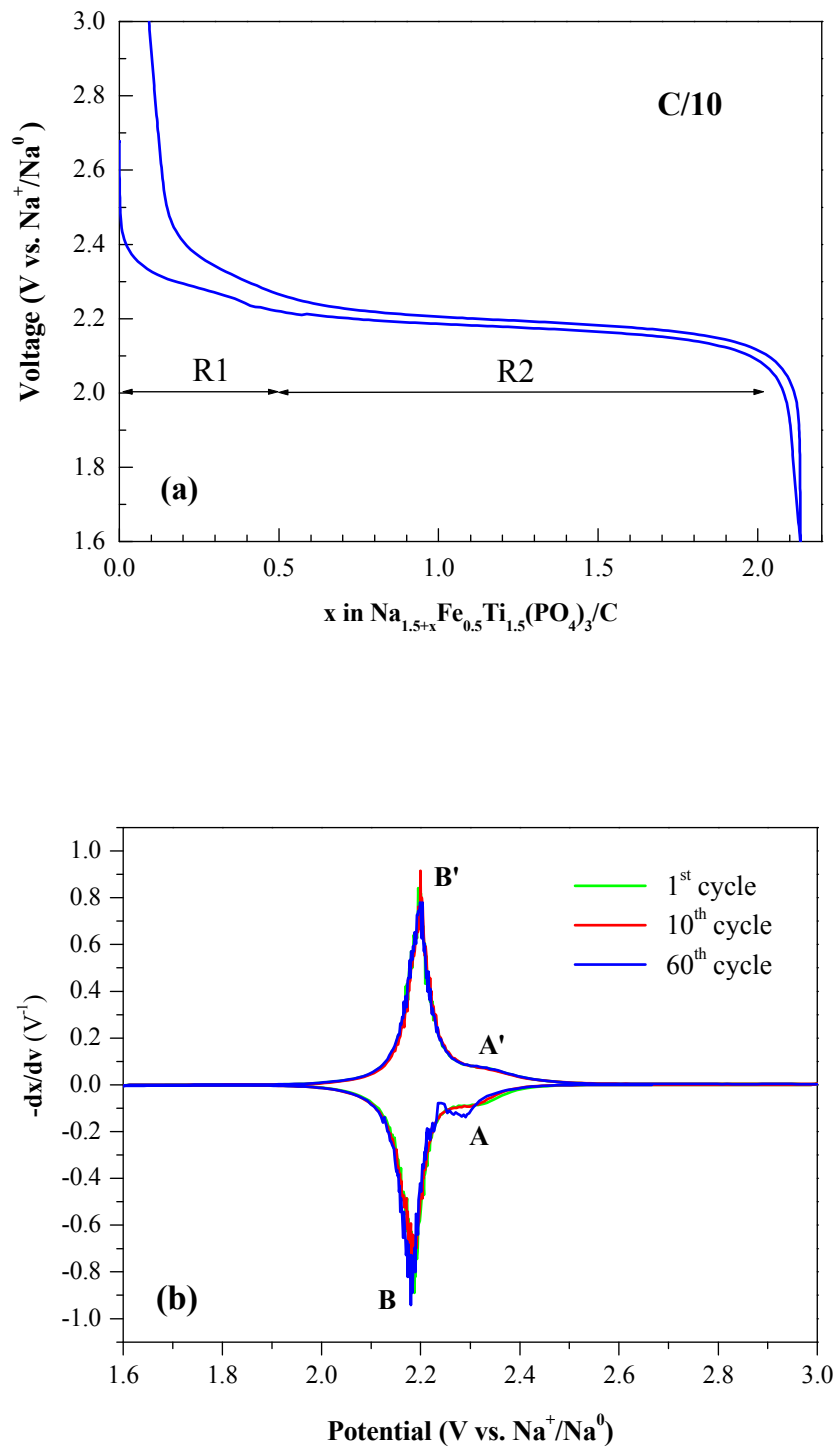


Figure 9

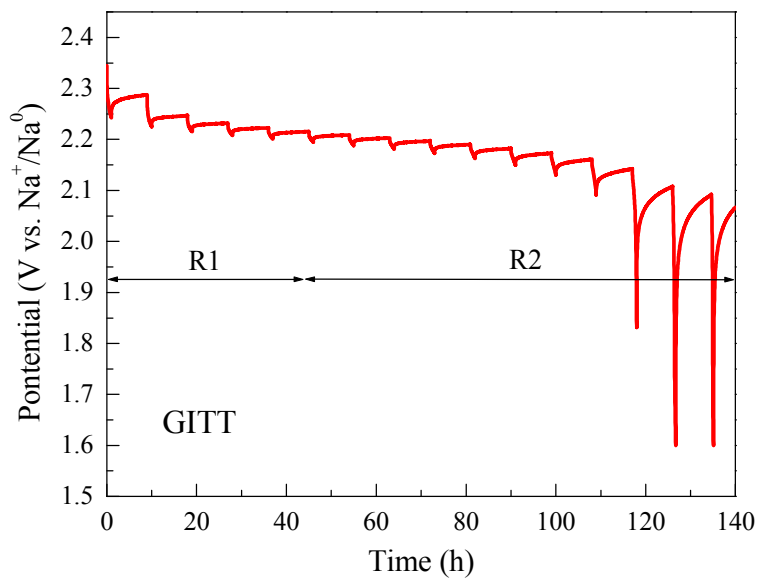


Figure 10

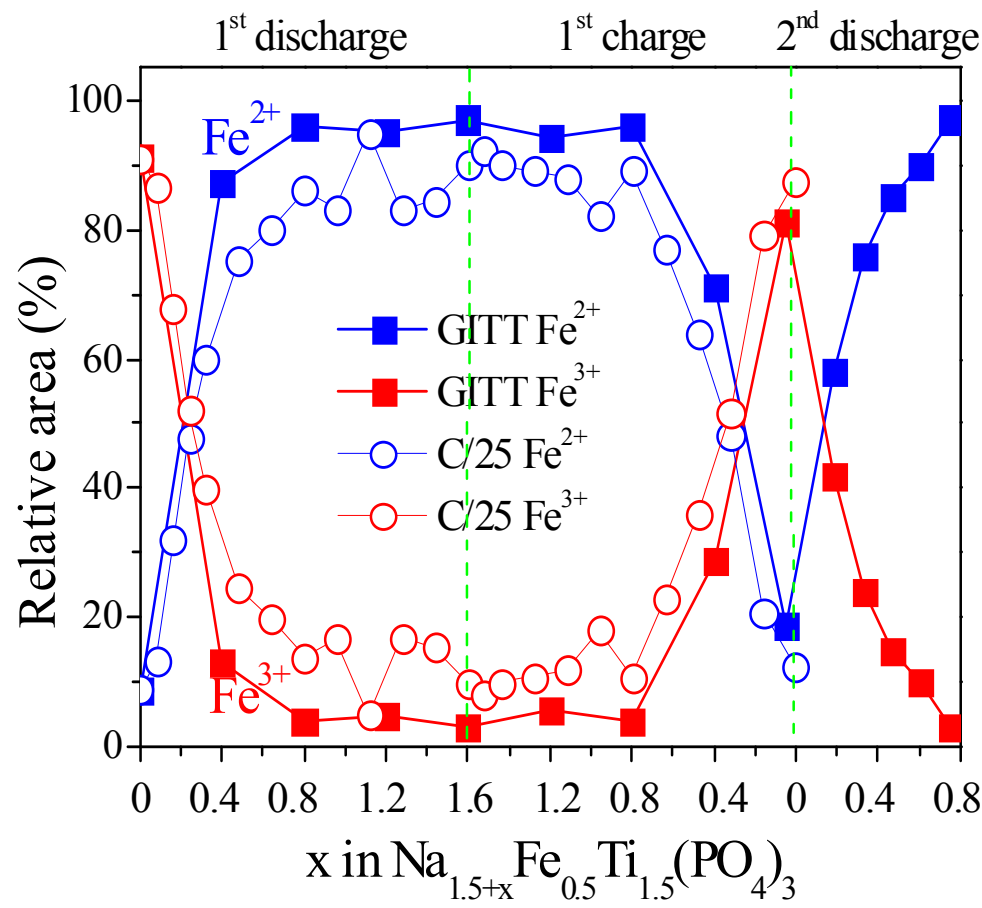


Figure 11

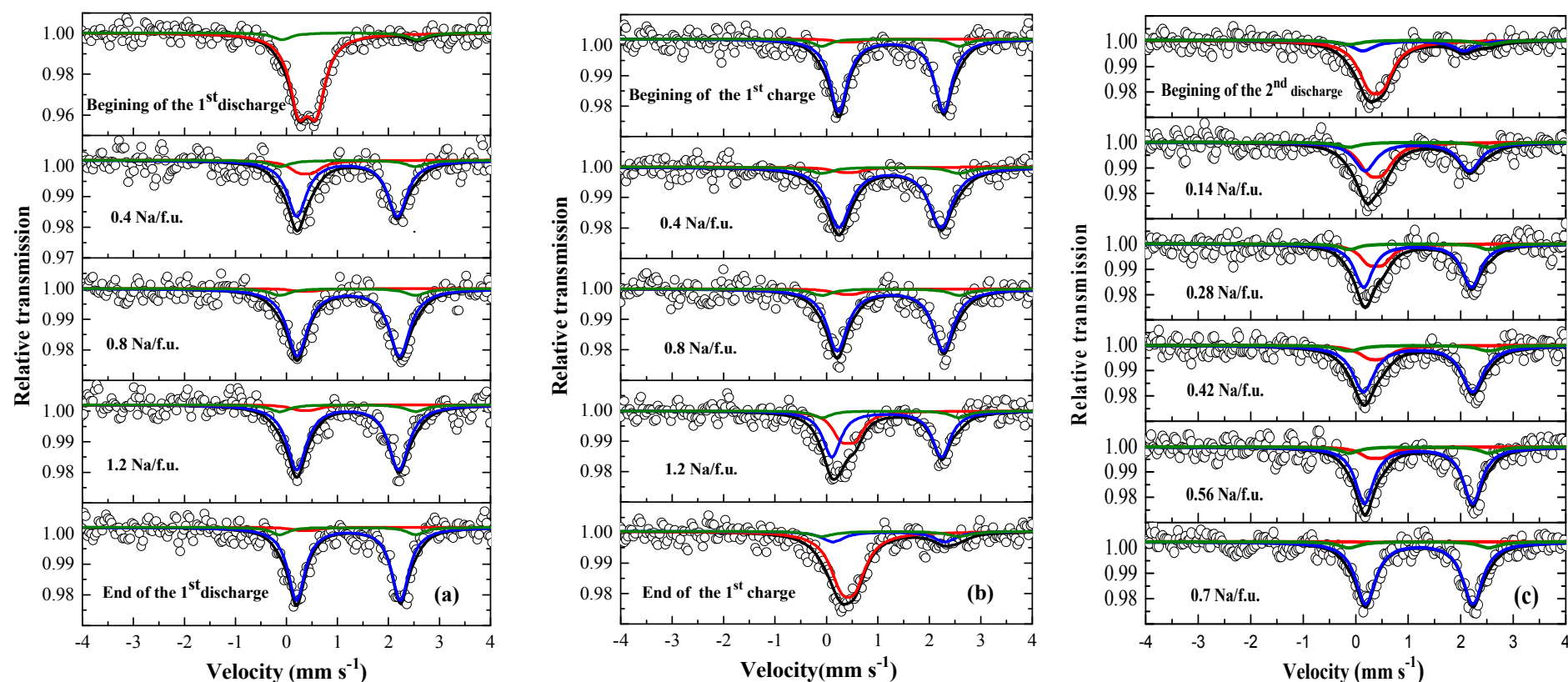


Figure 12

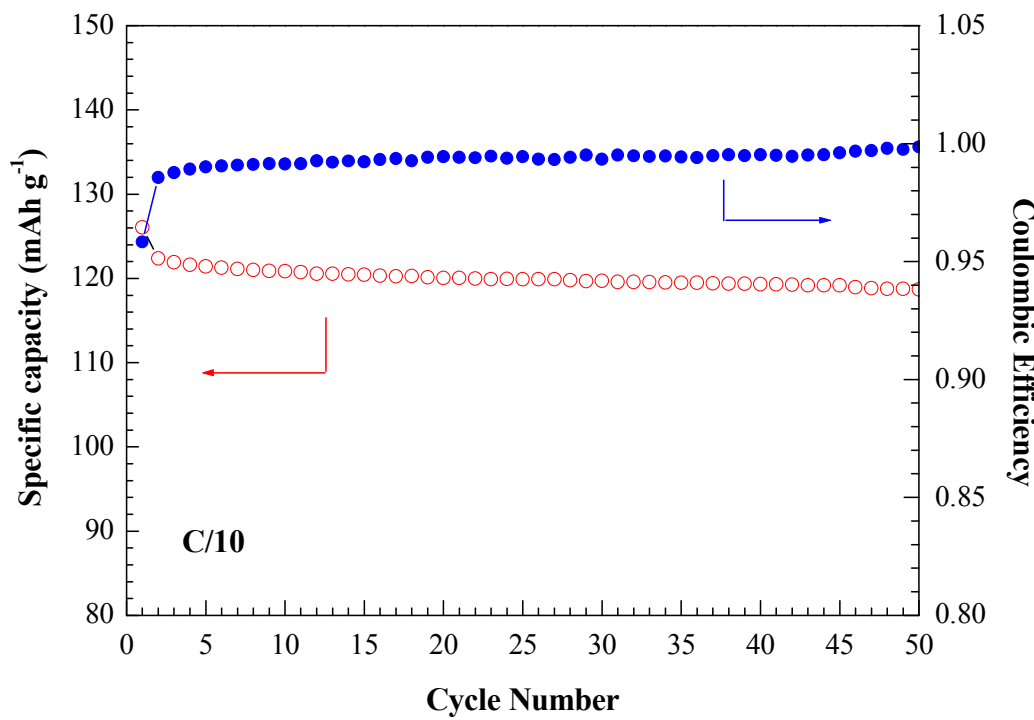
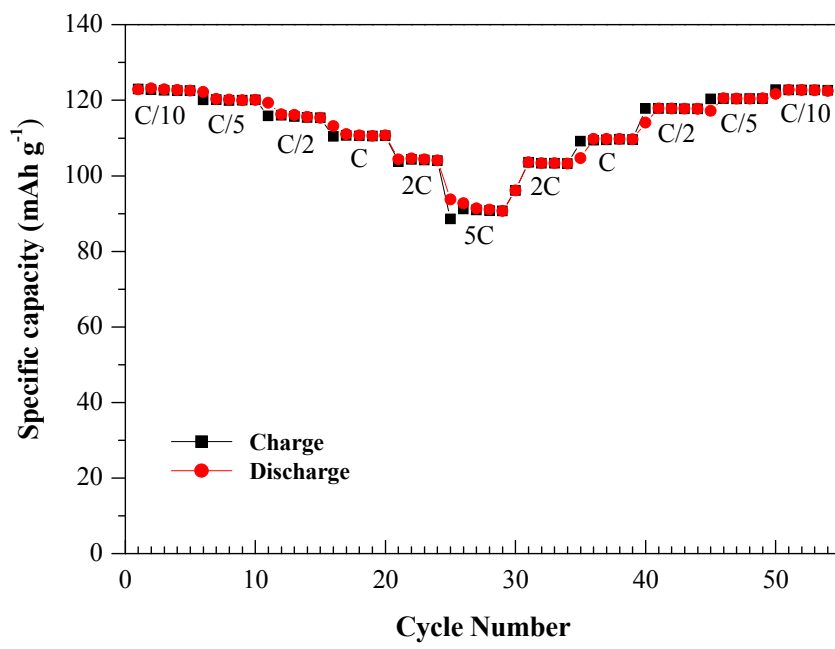


Figure 13



TOC / ABSTRACT GRAPHICS

